2016

The Impacts of Dry Dynamic Cores on Asymmetric Hurricane Intensification

Guimond, Stephen R.

American Meteorological Society

Guimond, S., J. Reisner, S. Marras, and F. Giraldo, 2016: THE IMPACTS OF DRY DYNAMIC CORES ON ASYMMETRIC HURRICANE INTENSIFICATION. J. Atmos. Sci.

The Impacts of Dry Dynamic Cores on Asymmetric Hurricane Intensification

STEPHEN R. GUIMOND

Earth System Science Interdisciplinary Center, University of Maryland, College Park, College Park, Maryland

JON M. REISNER

Los Alamos National Laboratory, Los Alamos, New Mexico

SIMONE MARRAS[a] AND FRANCIS X. GIRALDO

Department of Applied Mathematics, Naval Postgraduate School, Monterey, California

(Manuscript received 15 February 2016, in final form 16 August 2016)

ABSTRACT

The fundamental pathways for tropical cyclone (TC) intensification are explored by considering axisymmetric and asymmetric impulsive thermal perturbations to balanced, TC-like vortices using the dynamic cores of three different nonlinear numerical models. Attempts at reproducing the results of previous work, which used the community WRF Model, revealed a discrepancy with the impacts of purely asymmetric thermal forcing. The current study finds that thermal asymmetries can have an important, largely positive role on the vortex intensification, whereas other studies find that asymmetric impacts are negligible.

Analysis of the spectral energetics of each numerical model indicates that the vortex response to asymmetric thermal perturbations is significantly damped in WRF relative to the other models. Spectral kinetic energy budgets show that this anomalous damping is primarily due to the increased removal of kinetic energy from the vertical divergence of the vertical pressure flux, which is related to the flux of inertia–gravity wave energy. The increased kinetic energy in the other two models is shown to originate around the scales of the heating and propagate upscale with time from nonlinear effects. For very large thermal amplitudes (50 K), the anomalous removal of kinetic energy due to inertia–gravity wave activity is much smaller, resulting in good agreement between models.

The results of this paper indicate that the numerical treatment of small-scale processes that project strongly onto inertia–gravity wave energy can lead to significant differences in asymmetric TC intensification. Sensitivity tests with different time integration schemes suggest that diffusion entering into the implicit solution procedure is partly responsible for the anomalous damping of energy.

1. Introduction

The dynamics of tropical cyclones (TCs) can be broken down into two main groups relative to the storm center: axisymmetric and asymmetric. Although observations show that the total wind and vorticity fields of a TC are largely axisymmetric (e.g., Reasor et al. 2000), the latent heat forcing from deep convective clouds is often asymmetric (e.g., Guimond et al. 2011), with localized pulses containing both an azimuthal-mean heating component and a spectrum of higher-order azimuthal wavenumbers.

In the axisymmetric framework, the projection of localized heat forcing onto the azimuthal mean results in rings of heating typically maximized inside the radius of maximum winds for intensifying storms (e.g., Shapiro and Willoughby 1982). These heating rings drive an axisymmetric secondary circulation with radial inflow at low levels, updrafts through the core of the heating and radial outflow aloft. In the azimuthal mean, the vortex intensifies through the radial convergence of absolute angular momentum, which is materially conserved above the boundary layer. This framework has been understood for many years (e.g., Eliassen 1951; Shapiro and Willoughby 1982). Other axisymmetric theories for TC intensification

[a] Current affiliation: Department of Geophysics, Stanford University, Stanford, California.

Corresponding author address: Stephen R. Guimond, ESSIC, University of Maryland, College Park, 5825 University Research Ct. #4001, College Park, MD 20740.
E-mail: sguimond@umd.edu

DOI: 10.1175/JAS-D-16-0055.1

have been presented, such as the work of Emanuel (1986) and Rotunno and Emanuel (1987), which focus on the cycling of energy extracted from the thermodynamic disequilibrium at the air–ocean interface.

While considerable insight has been gained from axisymmetric theory, asymmetries associated with vortex Rossby waves, potential vorticity (PV) mixing, and vortical hot towers have been shown to be integral to TC intensity and structure change (e.g., Montgomery and Kallenbach 1997; Schubert et al. 1999; Montgomery et al. 2006), yet they can only be parameterized in axisymmetric numerical models. In a recent study, Persing et al. (2013) analyzed the axisymmetric and asymmetric dynamics of TCs to answer a basic question: How different is TC dynamics in three-dimensional and axisymmetric numerical models? A key result from their study indicates that the resolved, three-dimensional eddy processes associated with deep, vortical convection can assist the azimuthal-mean vortex intensification through upgradient radial momentum fluxes. Consequently, eddy parameterizations in axisymmetric models are not completely correct because they are assumed to act diffusively, transporting momentum in the downgradient direction only. The results of Persing et al. (2013) appear to stand in contrast to a similar study by Yang et al. (2007), where asymmetric eddy processes were found to reduce the intensity of the azimuthal-mean vortex, indicating an overall downgradient impact.

A fundamental part of asymmetric vortex dynamics in the presence of forcing is the "axisymmetrization" process. Early studies of the barotropic, nondivergent vorticity equation using a pseudospectral model by Melander et al. (1987) described how an initially elliptical vortex developed filaments (asymmetries) that decayed over time and lead to an end state that relaxes to an axisymmetric structure.

The studies of Smith and Montgomery (1995) and Montgomery and Kallenbach (1997) extended the work of Melander et al. (1987) by explaining more of the dynamics behind the axisymmetrization process and applying the theory to TCs. Physically, a perturbation introduced into a TC-like vortex will be sheared apart by the differential rotation creating alternating-signed bands of vorticity that interact with the mean flow through eddy momentum and heat fluxes, causing intensification (for upgradient transport) episodes in TCs (Montgomery and Kallenbach 1997; Montgomery and Enagonio 1998). The above studies showed that asymmetric perturbations can have an important, positive impact on vortex development and intensification, which is fundamentally distinct from that of axisymmetric mechanisms.

In a series of recent papers, Nolan and Montgomery (2002, hereafter NM02), Nolan and Grasso (2003, hereafter NG03), and Nolan et al. (2007, hereafter NMS07) studied the three-dimensional dynamics of idealized, small-amplitude, axisymmetric and asymmetric temperature/heating perturbations to baroclinic vortices modeled after realistic TCs. For localized heating, these studies found that the transformation of energy from the perturbations to the azimuthal-mean vortex is dominated by the projection of the heating onto the axisymmetric mode, with pure asymmetries having a negligible, largely negative impact on intensification. This result is in contrast with the work mentioned above on the barotropic axisymmetrization of nondivergent vorticity perturbations (Smith and Montgomery 1995; Montgomery and Kallenbach 1997; Nolan and Farrell 1999) and the three-dimensional analog using balanced PV perturbations (Montgomery and Enagonio 1998).

The essential difference of the Nolan et al. studies is that a baroclinic vortex along with temperature/heating perturbations was considered instead of using barotropic vortices with vorticity or PV perturbations in balanced models. The NG03 paper showed that the use of nonhydrostatic temperature perturbations in a baroclinic base state leads to the formation of an upshear tilt configuration of the PV anomalies, which extract energy from the mean vortex through downgradient eddy momentum fluxes (e.g., Farrell 1982). Although some of the energy contained in the perturbations is returned to the vortex through axisymmetrization (upgradient eddy momentum fluxes), there is typically a net sink of energy in the vortex of negligible magnitude (NG03; NMS07). The NG03 results were computed using a linear, anelastic model and verified using a nonlinear, compressible code: the dynamic core of the Weather Research and Forecasting (WRF) Model (version 1.2.1).

The studies described above indicate that uncertainty exists in our knowledge of the impacts of asymmetric processes in TC dynamics. Attempts to reproduce the work of NG03 with three different nonlinear numerical models revealed major discrepancies with the impacts of asymmetric thermal forcing. As a result, the goal of the present paper is to document these differences and analyze in detail the dynamical and numerical reasons for this discrepancy. The impacts of the axisymmetric and asymmetric modes in TC dynamics are discussed in light of these results, with potential implications for the prediction of hurricane intensity and structure change.

2. Description and setup of numerical models

a. *The WRF Model*

The WRF Model solves the compressible, nonhydrostatic Euler equations written in conservative form with a mass vertical coordinate η that is defined by a normalized

hydrostatic pressure (Laprise 1992). A detailed description of WRF is presented in Skamarock and Klemp (2008) and Skamarock et al. (2008), and here we comment on the most important elements of the algorithm. Note that we are using version 3.1.1 of the model, but the dynamic core is essentially the same as that used in NG03 (version 1.2.1), which used a height vertical coordinate.

The simulations presented here are idealized on an f plane and using exponentially stretched η levels, which results in approximately constant vertical spacing of these levels in height. To account for the small differences between η and height, all model output is interpolated to height levels. The simplified model equations for a dry atmosphere using a Laplacian operator for explicit diffusion and η as the vertical coordinate can be expressed as follows:

$$\frac{\partial \mu u}{\partial t} + \nabla \cdot \mu \mathbf{u} u = -\frac{\mu}{\rho}\frac{\partial p'}{\partial x} + f\mu v + \mu\kappa\nabla^2 u, \quad (1a)$$

$$\frac{\partial \mu v}{\partial t} + \nabla \cdot \mu \mathbf{u} v = -\frac{\mu}{\rho}\frac{\partial p'}{\partial y} - f\mu u + \mu\kappa\nabla^2 v, \quad (1b)$$

$$\frac{\partial \mu w}{\partial t} + \nabla \cdot \mu \mathbf{u} w = g\left(\frac{\partial p'}{\partial \eta} - \mu'\right) + \mu\kappa\nabla^2 w, \quad (1c)$$

$$\frac{\partial \mu \theta}{\partial t} + \nabla \cdot \mu \mathbf{u} \theta = \mu\kappa\nabla^2\theta', \quad \text{and} \quad (1d)$$

$$\frac{\partial \mu'}{\partial t} + \nabla \cdot \mu \mathbf{u} = 0, \quad (1e)$$

where $\mathbf{u} = (u, v, w)$ is the three-dimensional velocity vector, $\mu = \mu(x, y)$ is the mass per unit area within a column, θ is the potential temperature, ρ is the dry air density, p is the pressure, f is the Coriolis parameter, g is gravity, κ is the eddy viscosity/diffusivity, and ∇ is the three-dimensional gradient operator.[1] The prime notation over certain variables denotes deviations from the hydrostatically balanced reference state, which are three-dimensional quantities. Note that comparisons between WRF, version 3.1.1 (mass coordinate), and WRF, version 1.2.1 (height coordinate), for the NG03 problem studied here were conducted. These comparisons produced nearly the exact same results, likely because of the very small differences between η and height.

The discrete model employs a spatially staggered Arakawa C grid in the horizontal and vertical directions, with velocities located on the cell faces and scalars defined at cell centers [except for geopotential, which is defined at cell faces in the vertical and appears in the full model equations (Skamarock and Klemp 2008)]. To compute coupled terms in the discrete model, averaging of scalars to cell faces is required, which adds damping into the solutions.

The horizontal nonlinear advective terms are typically computed with a fifth-order upwind biased discretization, which contains a diffusion term with a coefficient proportional to the Courant number (Wicker and Skamarock 2002). We also examined tests with a sixth-order operator, which has a centered discretization and thus no added diffusion. The vertical advective terms are calculated with a third-order upwind scheme that also contains a diffusion term of the next higher order. The use of the even-ordered operators did not have much of an effect on the results of this study. Therefore, we chose to use the fifth-order scheme in the horizontal and the third-order scheme in the vertical, which is recommended by the WRF developers.

A split-explicit time integration method is used in WRF, where fast time scales, such as acoustic and gravity wave modes, are handled on a small time step and slower time scales, such as advection, are computed on a larger time step (e.g., Klemp and Wilhelmson 1978; Wicker and Skamarock 2002; Skamarock and Klemp 2008). Within the small time step, horizontal modes are treated explicitly, while vertical modes are implicitly solved. A third-order Runge–Kutta-type scheme is used to perform the time discretization that incorporates both the small– and large–time step equations. The small–time step results are applied as a correction to the large time step calculations during the Runge–Kutta time integration. See Skamarock and Klemp (2008) for details on the time integration sequence.

The WRF Model has a few flags in the input file that control, to some extent, the level of dissipation in the solutions. Our goal is to analyze minimally dissipative WRF solutions, so we have *not* used explicit sixth-order numerical filtering, vertical velocity damping, divergence damping, or external mode damping. Explicit diffusion at the model top and through the Laplacian operator in Eqs. (1a)–(1d) are discussed in section 2d. Table 1 provides a quick reference for the default numerical schemes used in this study.

b. *The HIGRAD model*

The High Gradient (HIGRAD) model also solves the compressible, nonhydrostatic Euler equations written in conservative (flux) form only using a height vertical coordinate. The simplified model equations for the idealizations described above can be written as follows:

[1] Technically the vertical derivatives are with respect to η here, but the differences between η and height are very small for this problem. The vertical derivatives in the gradient operator are with respect to height elsewhere.

TABLE 1. Summary of default numerical schemes used in each model for this study. See text for details.

	HIGRAD	WRF	NUMA
Time integration	Semi-implicit with forward Euler	Split-explicit with Runge–Kutta	Semi-implicit with leapfrog
Spatial discretization	Finite difference on A grid	Finite difference on C grid	Spectral element
Advection	QUICK	Fifth-order horizontal, third-order vertical	Spectral element
Explicit filters	Sixth-order spatial	—	First-order temporal

$$\frac{\partial \rho u}{\partial t} + \nabla \cdot \rho \mathbf{u} u = -\frac{\partial p'}{\partial x} + f\rho v + \rho\kappa\nabla^2 u, \quad (2a)$$

$$\frac{\partial \rho v}{\partial t} + \nabla \cdot \rho \mathbf{u} v = -\frac{\partial p'}{\partial y} - f\rho u + \rho\kappa\nabla^2 v, \quad (2b)$$

$$\frac{\partial \rho w}{\partial t} + \nabla \cdot \rho \mathbf{u} w = -\frac{\partial p'}{\partial z} - \rho' g + \rho\kappa\nabla^2 w, \quad (2c)$$

$$\frac{\partial \rho \theta}{\partial t} + \nabla \cdot \rho \mathbf{u} \theta = \rho\kappa\nabla^2 \theta', \quad \text{and} \quad (2d)$$

$$\frac{\partial \rho}{\partial t} + \nabla \cdot \rho \mathbf{u} = 0. \quad (2e)$$

The discrete forms of Eqs. (2a)–(2e) can be found in Reisner et al. (2005), although in that paper a stress tensor was used to model subgrid-scale turbulent diffusion in the momentum equations instead of the Laplacian operator used here. The discretized equations utilize an unstaggered Arakawa A grid in the horizontal and vertical directions with all variables defined at cell centers.

The advective and turbulent fluxes appearing in the above equations are computed on a cell face. The advective fluxes are computed with the second-order accurate quadratic upstream interpolation for convective kinematics (QUICK; Leonard and Drummond 1995) scheme in both the horizontal and vertical directions. Other advection schemes can be implemented in HIGRAD, and we have tested the use of a first-order accurate upwind scheme for the present simulations as well. We use QUICK as the default advection scheme and will make note where departures from this practice are made.

The pressure gradient force is computed using second-order centered finite differences, which can result in two-grid interval noise when computed on the A grid. Care is taken to address the possibility of noise by conducting sensitivity tests with the first-order upwind advection scheme, which is highly diffusive, and implementing a sixth-order explicit numerical filter in the horizontal directions into the model.

The filter is incorporated into HIGRAD by adding an additional term to the right-hand sides of Eqs. (2a)–(2d) following Xue (2000). Using the zonal momentum equation as an example,

$$\frac{\partial \rho u}{\partial t} = \mathrm{RHS} + \alpha \nabla_h^6 \rho u, \quad (3)$$

where RHS denotes all terms on the right-hand side of Eq. (2a) in addition to the advective flux, ∇_h^6 is the sixth-order horizontal diffusion operator, and α is a coefficient that determines the strength of the filter response. The discrete form of the sixth-order filter in Eq. (3) can be written

$$\alpha \nabla_h^6 \rho u = \alpha \left(\frac{F_{i+1/2} - F_{i-1/2}}{\Delta x} + \frac{F_{j+1/2} - F_{j-1/2}}{\Delta y} \right), \quad (4)$$

where

$$F_{i+1/2} = \rho_{i+1/2}[10(u_{i+1} - u_i) - 5(u_{i+2} - u_{i-1}) + u_{i+3} - u_{i-2}] \quad \text{and} \quad (5)$$

$$F_{i-1/2} = \rho_{i-1/2}[10(u_i - u_{i-1}) - 5(u_{i+1} - u_{i-2}) + u_{i+2} - u_{i-3}] \quad (6)$$

are the fifth-order momentum fluxes in the x direction valid at the cell faces, which have second-order accuracy. The y-direction fluxes have a similar form. Note that, in order to achieve values of the fluxes that are comparable in magnitude to other terms in Eqs. (2a)–(2d), the scaling by Δx^5 that should appear in Eqs. (5) and (6) is suppressed. High-frequency oscillations are possible with the application of the sixth-order filter, so we have followed Xue (2000) and set the fluxes in Eqs. (5) and (6) to zero whenever they have a different sign than the gradient of the quantity on which the operator is acting. This simple flux-limiting procedure ensures monotonicity of the filter.

The coefficient α is defined following Knievel et al. (2007):

$$\alpha = 2^{-6} s^{-1} \Delta t^{-1} \beta, \quad (7)$$

where s is the number of times the filter is applied, which is 2 here (once in each horizontal direction), Δt is the time step (described below), and β determines the strength of the damping of two-grid interval waves (0.0 for no damping and 1.0 for maximum damping). Here we used a value of 1.0 to examine the sensitivity of the HIGRAD simulations to small-scale noise. These sensitivity tests showed that the filter effectively damps energy within the $6\Delta x$–$7\Delta x$ region, with the larger scales,

including those associated with the heating and vortex, left unaffected. The filter with $\beta = 1.0$ is included in all HIGRAD simulations presented in this paper.

The HIGRAD model is capable of using several different time integration schemes in the discrete solver. Here, we use a semi-implicit solution procedure with first-order forward Euler time differencing as our default method. The semi-implicit approach in HIGRAD solves for the fast modes in a coupled, three-dimensional fashion using only an implicit solver. The details of the semi-implicit algorithm in HIGRAD can be found in the appendix of Reisner et al. (2005). We have also implemented a fully explicit, standard third-order Runge–Kutta scheme into HIGRAD to examine the sensitivity of the solutions to time integration method and accuracy for the problem presented in this study.

In summary, the default HIGRAD numerical algorithms used in this paper are the QUICK scheme for advection and the semi-implicit time integration approach along with the sixth-order numerical filter. Departures from these default settings will be noted where appropriate. Table 1 provides a quick reference for the default numerical schemes used in this study.

c. NUMA

The Nonhydrostatic Unified Model of the Atmosphere (NUMA) solves a similar equation set as HIGRAD, but the advective terms are written in nonconservative (advective) form. The simplified model equations for the idealizations described above can be written as follows:

$$\frac{\partial u}{\partial t} + \mathbf{u}\cdot\nabla u = -\frac{1}{\rho}\frac{\partial p'}{\partial x} + fv + \kappa\nabla^2 u, \tag{8a}$$

$$\frac{\partial v}{\partial t} + \mathbf{u}\cdot\nabla v = -\frac{1}{\rho}\frac{\partial p'}{\partial y} - fu + \kappa\nabla^2 v, \tag{8b}$$

$$\frac{\partial w}{\partial t} + \mathbf{u}\cdot\nabla w = -\frac{1}{\rho}\frac{\partial p'}{\partial z} - \frac{\rho'}{\rho}g + \kappa\nabla^2 w, \tag{8c}$$

$$\frac{\partial \theta'}{\partial t} + \mathbf{u}\cdot\nabla\theta = \kappa\nabla^2\theta', \quad \text{and} \tag{8d}$$

$$\frac{\partial \rho}{\partial t} + \nabla\cdot\rho\mathbf{u} = 0, \tag{8e}$$

where it has been assumed that the background/reference pressure is in hydrostatic balance. The discrete forms of these equations can be found in Giraldo and Restelli (2008) for a two-dimensional model and in Kelly and Giraldo (2012) for a three-dimensional explicit model. A flux form version of the equations is available in NUMA, but this is not expected to make a significant difference here because the error incurred from using the advective form is much lower than the temporal error, which dominates the solutions (Giraldo and Restelli 2008; Kelly and Giraldo 2012).

The spatial discretization of Eqs. (8a)–(8e) is performed using the spectral element technique, which is outlined in detail by Giraldo and Restelli (2008) and Kelly and Giraldo (2012). For brevity, we only outline the most important elements of the algorithm. In the spectral element method, the model domain is decomposed into a set of nonoverlapping hexahedral elements. Within each element, a prognostic variable is represented by polynomial expansion using Lagrange basis functions of a chosen order (see next section for details). The continuous spatial derivatives found in Eqs. (8a)–(8e) are constructed in discrete form by taking the derivatives of the polynomial basis functions analytically. The prognostic variables are solved and stored at collocated nodal grid points similar to the Arakawa A grid. Note that the nodal grid points within each element are not equally spaced (Legendre–Gauss–Lobatto points are used), and the model output is interpolated to a grid with uniform spacing for analysis (see next section).

The NUMA time integration strategy used in this paper is based on the three-dimensional semi-implicit approach outlined in Giraldo et al. (2013). Several different time discretization methods with various orders of accuracy and levels of temporal diffusion are available in the model. In this paper, we chose to analyze second-order leapfrog time differencing (LF2) and a second-order additive Runge–Kutta (ARK2B) method to bracket the amount of temporal diffusion in the solutions. The LF2 method requires the use of a Robert–Asselin time filter for stability, which reduces the accuracy of the method to first order because of the substantial temporal diffusion. On the other hand, ARK2B with the free-parameter $a_{32} = 0.5$ (Giraldo et al. 2013) is the least dissipative second-order NUMA time integrator. In the remainder of the paper, we use the LF2 method as the default time integrator in NUMA and compare it with ARK2B where appropriate. Table 1 provides a quick reference for the default numerical schemes used in this study.

d. Setup and initial conditions

The setup of all three models is the same and follows most of the same settings as NG03. This includes a dry atmosphere with no surface dissipation (free slip at the lower boundary) and a constant Coriolis parameter of $5.0 \times 10^{-5}\,\mathrm{s}^{-1}$. Doubly periodic horizontal boundary conditions are used in all models. Gravity waves are damped at the model top using a Rayleigh absorbing layer (Skamarock et al. 2008):

$$\tau(z) = \gamma \sin^2\left[\frac{\pi}{2}\left(1 - \frac{z_{\mathrm{top}} - z}{z_d}\right)\right], \tag{9}$$

where γ is a coefficient determining the strength of the damping (we chose a value of 0.008 33), z_{top} is the top of

the model (20 km), z_d is the depth of the damping layer (4 km), and z is the height.

The model domain covers 800 km in both horizontal directions with 2-km grid spacing in WRF and HIGRAD. The first model level is located at 167 m with constant vertical spacing of 333 m extending up to 20-km height for a total of 60 levels. In NUMA, we have chosen to use fifth-order polynomial basis functions, 80 elements in each horizontal direction, and 12 elements in the vertical. These choices yield an effective resolution of ~2 km in the horizontal and ~333 m in the vertical, matching the grid spacing of WRF and HIGRAD. The eddy diffusivities found in Eqs. (1a)–(1d), (2a)–(2d), and (8a)–(8d) are set to constant values of 150 $m^2 s^{-1}$ in both the horizontal and vertical directions. The NG03 study also used constant eddy diffusivities, although with smaller values. Sensitivity tests in each model with smaller values in all directions, as well as smaller values in the vertical direction only, did not alter the qualitative results or conclusions drawn.

The initial conditions in all three models are as follows. The basic-state vortex is very similar to the tropical storm–like vortex used in NG03 and NMS07. Initially, we used the exact same tropical storm–like vortex as NG03 and NMS07[2], but that vortex had small, albeit nonnegligible, velocities on the domain edges, which could cause a problem with the doubly periodic boundary conditions. To avoid these potential problems, a vortex with a slightly steeper radial decay function than the original vortex was used to ensure a wide region of zero velocities at the domain edges. This vortex has an analytical form similar to that given in NMS07, but with an added radial decay function to force the velocities to zero at far radii:

$$\overline{v}(r,z) = V(r)\exp\left(-\frac{z^{\sigma}}{\sigma D_1^{\sigma}}\right)\exp\left[-\left(\frac{r}{D_2}\right)^6\right], \qquad (10)$$

where $\overline{v}$ is the azimuthal-mean tangential velocity, V is the surface tangential velocity (a function of radius r), $\sigma = 2.0$ and $D_1 = 5823$ m define the parameters of the barotropic portion of the vortex, and $D_2 = 200$ km. The surface tangential velocity is found by integrating a specified Gaussian vorticity distribution with peak vorticity at the vortex center of $1.5 \times 10^{-3}\ s^{-1}$ and maximum winds of 21.5 $m\,s^{-1}$ located at a radius of ~50 km (NG03 and NMS07).

Figures 1a and 1b show the structure of the basic-state vortex described above. In Fig. 1a, the surface azimuthal-mean tangential velocity of the original NG03 and NMS07 vortex is shown along with the new one used in this study. Figure 1b shows the vertical, baroclinic structure of the new vortex using the same vertical decay function as that described in NG03 and NMS07. Note that the vorticity profile of the basic-state vortex used in this study is identical to the one used in NG03 (see Fig. 2a in their paper).

The potential temperature and density fields that hold the vortex in thermal wind balance are found using an iterative procedure that oscillates between hydrostatic and gradient wind balance until a convergence criterion is met. This vortex initialization system is described in Nolan (2011). The initial environmental temperature profile comes from the Jordan (1958) mean hurricane season sounding with hydrostatic pressure being computed.

Two types of impulsive (initial condition) thermal perturbations were considered: an axisymmetric and a purely asymmetric (wavenumber 3) potential temperature anomaly. The Gaussian structures of these perturbations in the radius–height plane follow NM02 [their Eq. (5.1)] and are centered at a radius of 40 km and height of 5 km. Figures 1c and 1d show the structure of the wavenumber-3 anomaly in the horizontal and vertical planes, respectively. We first test a small-amplitude 1-K potential temperature perturbation to be consistent with the NM02 and NG03 studies. Larger amplitudes are examined later in the study.

As noted in NG03, explicit diffusion acts on the total velocity variables in WRF as well as HIGRAD and NUMA, which results in a slight spindown of the vortex over the course of the 6-h simulation. This is also true of diffusion inherent to the numerical scheme. To be consistent with the Nolan et al. studies, all model results are presented as perturbations: the difference between a simulation of the basic-state vortex plus the thermal anomaly and a simulation of only the basic-state vortex. This helps to identify the intensification signal for the small-amplitude perturbations.

3. Vortex response to thermal perturbations

a. *Small-amplitude results*

In this section, we examine comparisons between WRF, HIGRAD, and NUMA for small-amplitude, linear heating perturbations of 1 K like those used in NG03. Figure 2 shows the perturbation maximum wind speed evolution and the ratio between models (relative to WRF) at the lowest model level for the 1-K wavenumber-0 (WN0) and wavenumber-3 (WN3) perturbations with a 10-min output interval. Note that minimum pressure perturbations showed similar structure, but we present wind speeds because of the focus on kinetic energy throughout

[2] Note that use of the *exact* same vortex as these studies did not change the qualitative results of this paper or the conclusions drawn.

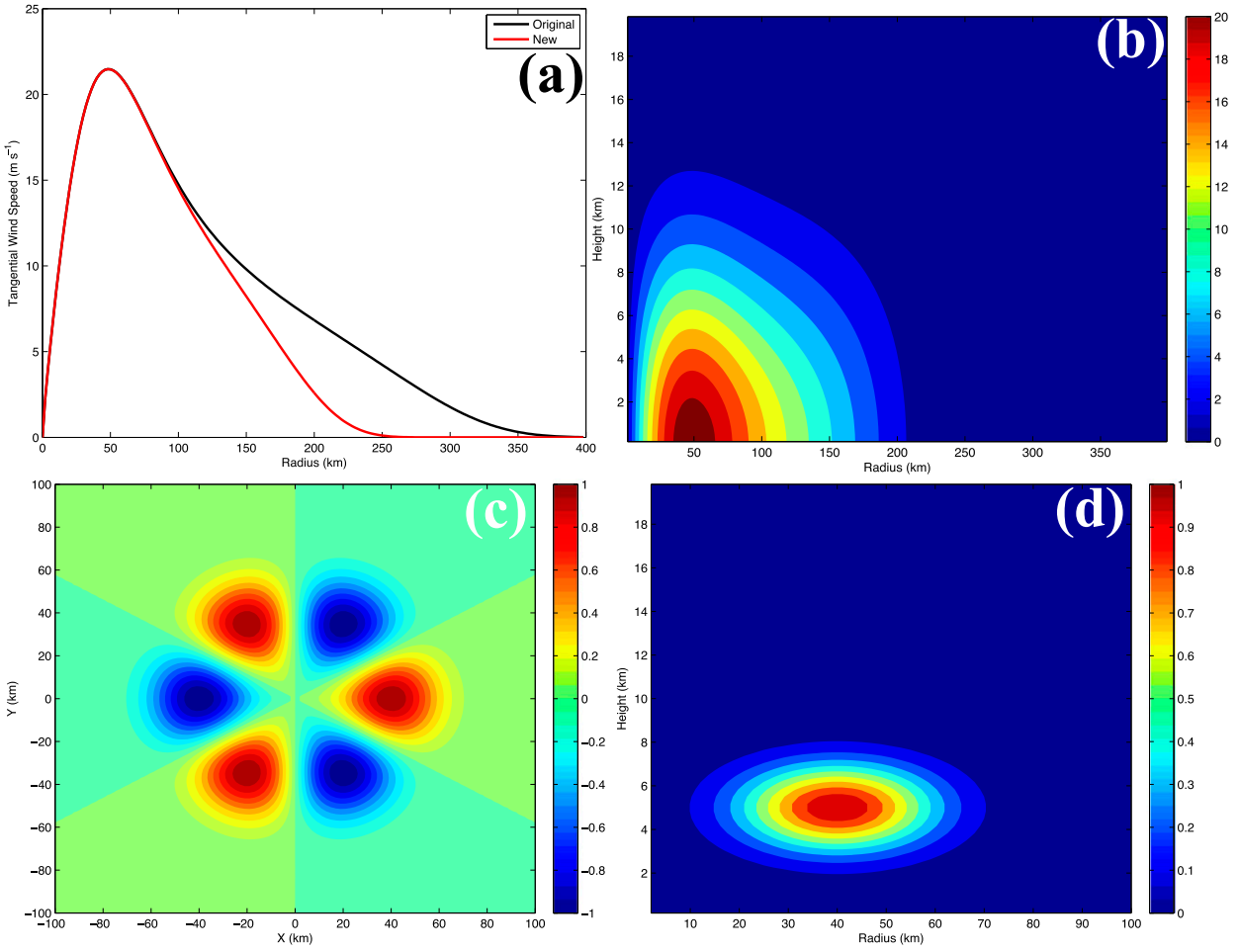

FIG. 1. Structure of the initial conditions used for the modeling experiments. Shown is (a) the surface tangential velocity field (m s^{-1}) of the original vortex used in NG03 and the new vortex used in this study, (b) the tangential velocity field (m s^{-1}) in the radius–height plane for the new vortex, (c) the 1-K WN3 potential temperature perturbation (K) in the horizontal plane, and (d) the 1-K WN3 potential temperature perturbation (K) in the radius–height plane for a positive anomaly.

the paper. For both perturbation types there is a roughly 1–2-h period of adjustment to the imposed temperature anomaly with the radiation of inertia–gravity waves and large oscillations in wind speed. At short and long times in the simulations, there is also a quasi-balanced vortex response to the forcing.

For the WN0 case, the forcing develops an axisymmetric secondary circulation, which leads to intensification of the vortex (positive values of perturbation wind speed; see Fig. 2a) through the radial convergence of absolute angular momentum (e.g., Shapiro and Willoughby 1982). Figures 2a and 2b show that all models agree well on this process, with maximum wind speed perturbation ratios hovering around 1 (Fig. 2b).

For the WN3 case, the forcing develops quasi-balanced PV anomalies that get sheared by the radial and vertical gradients in tangential velocity of the basic-state vortex. These PV waves interact with the vortex through eddy heat and momentum fluxes as part of the axisymmetrization process discussed in the introduction. Figures 3a–c show the vertical component of the perturbation PV at the level of peak heating (~5 km) at 0.5 h into the 1-K WN3 simulations for HIGRAD, WRF, and NUMA, respectively. The structures and magnitudes of the anomalies are very similar to each other, with only minor differences in the peak values (~10% or less). At this early time, lines of constant phase between the inner and outer rings of PV anomalies are tilting into the radial shear of angular velocity, which leads to an extraction of energy from the mean vortex and growth of the perturbations (NMS07). At 4 h into the simulations, the anomalies in each model (Figs. 3d–f) are also very similar, and they are tilting with the radial shear as they return energy to the mean vortex during axisymmetrization.

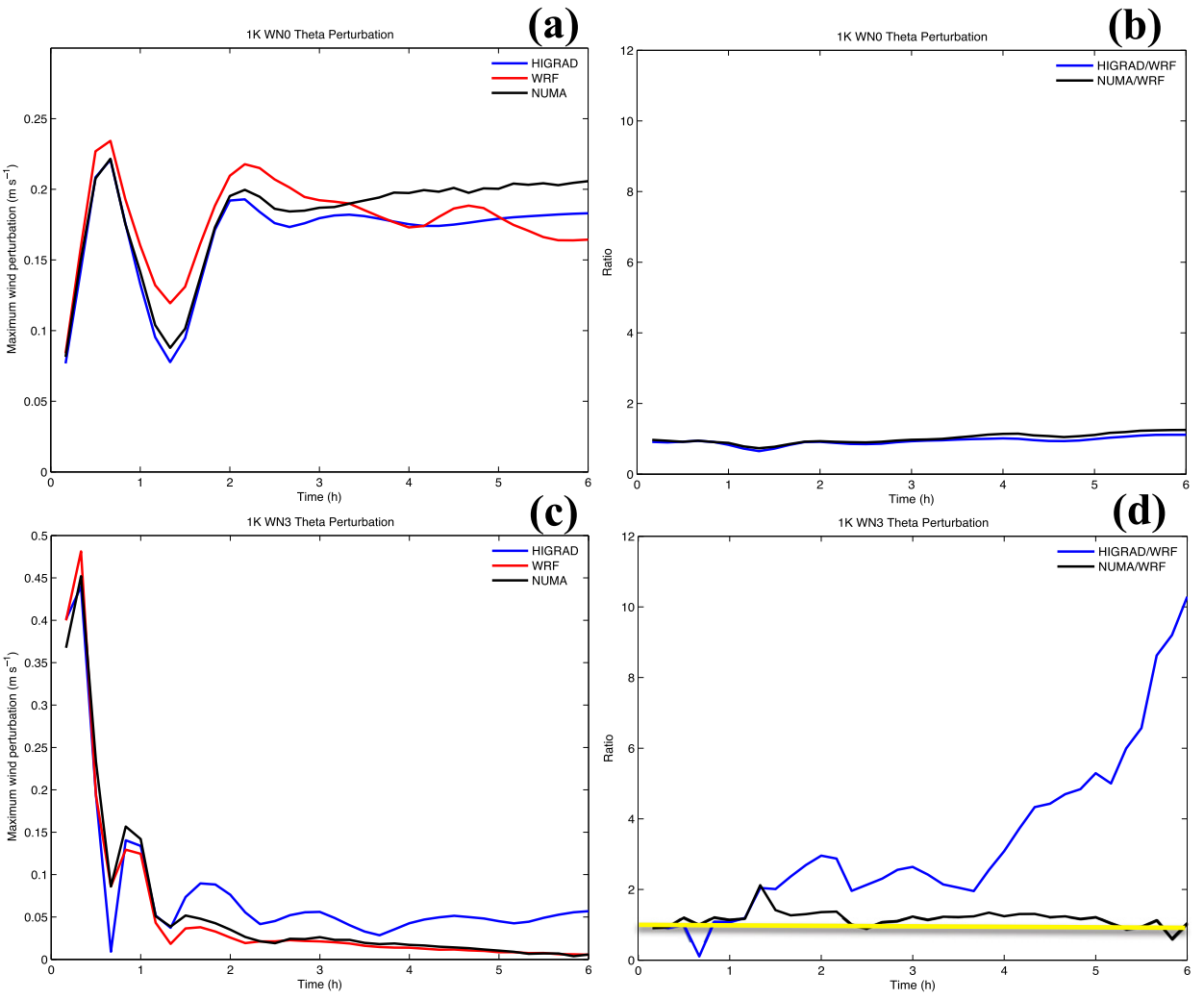

FIG. 2. Time series of (a),(c) maximum wind speed perturbation and (b),(d) maximum wind speed perturbation ratio relative to WRF for the (top) 1-K WN0 perturbation and the (bottom) 1-K WN3 perturbation. The results are reported at the lowest model level with a 10-min output interval. The yellow line in (d) helps to identify a ratio of one.

Figure 2c shows the wind speed perturbation results for the 1-K WN3 anomaly. There are differences in the adjustment dynamics at early times (0–2 h) between models, with results varying by a factor of ~2 until ~3.5 h (Fig. 2d). From ~3.5 h onward, the HIGRAD results show a slight increase in wind speed, while WRF and NUMA show a slight decrease in wind speed (Fig. 2c) that results in significant differences in wind speed ratio at later times (Fig. 2d). The HIGRAD results were computed with the semi-implicit time integration method and verified with a fully explicit third-order Runge–Kutta scheme, which produced very similar values. Note that all models show intensification of the vortex as a result of the 1-K WN3 thermal anomaly in terms of either maximum wind speeds (Fig. 2c) or minimum pressure (not shown).

Figures 4a–c show the perturbation horizontal wind speed fields averaged over the ~0–5-km layer at 1 h into the 1-K WN3 simulations for HIGRAD, WRF, and NUMA, respectively. A wavenumber-6 pattern in the wind speed is apparent at this time as each model adjusts to the imposed thermal asymmetry. The HIGRAD model produces larger wind speed magnitudes than WRF and NUMA for the inner-ring asymmetry with similar values to NUMA in the outer ring. The WRF Model produces the lowest wind speed magnitudes of all three models. At 4 h into the simulations (Figs. 4d–f), the results of the axisymmetrization process are clear, as the wind speeds have taken on an axisymmetric ringlike structure. The magnitudes are significantly higher in HIGRAD (Fig. 4d) than either WRF (Fig. 4e) or NUMA (Fig. 4f) at this time in the core of the vortex as well as in

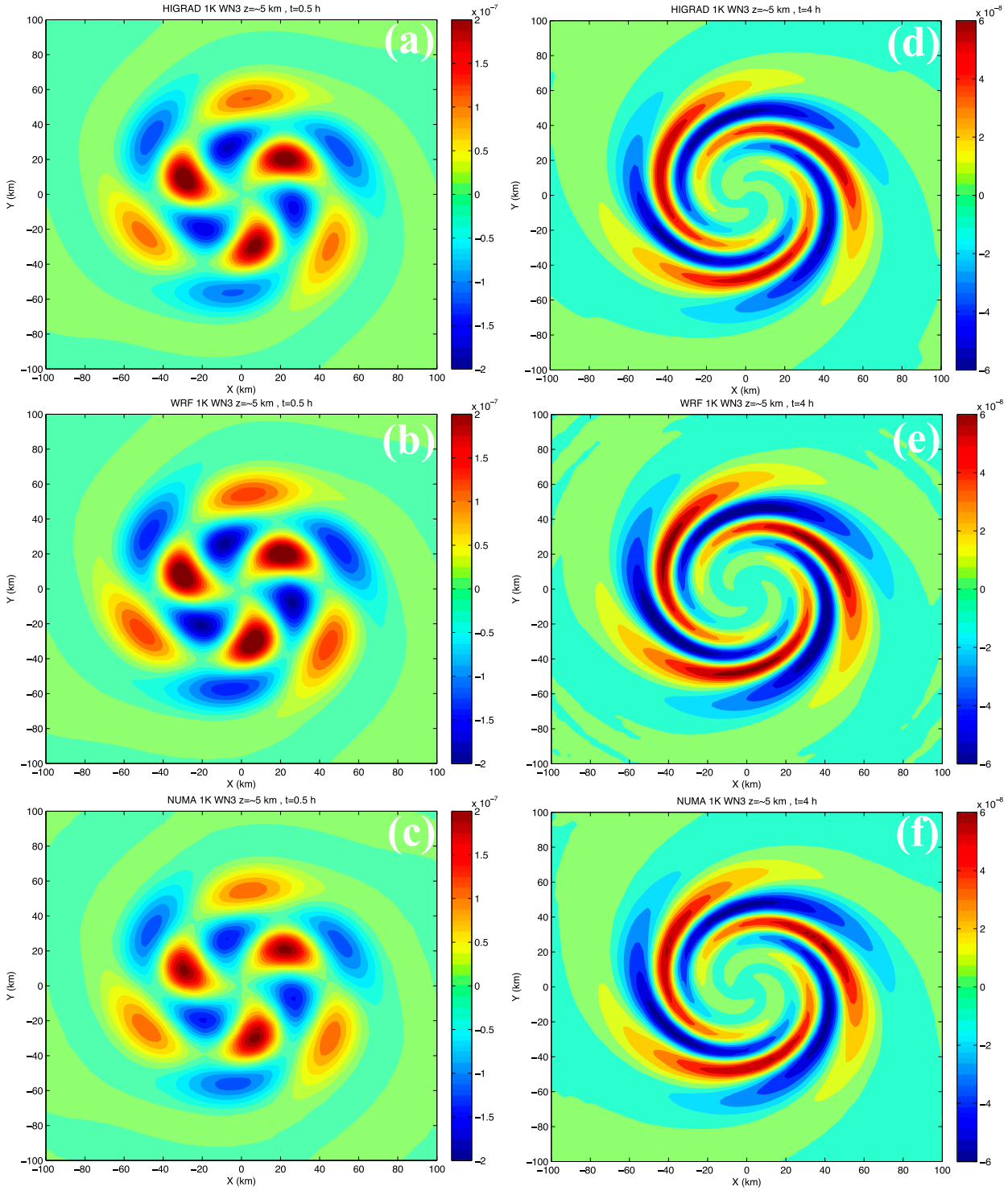

FIG. 3. Snapshots of the vertical component of perturbation potential vorticity (K m^2 kg^{-1} s^{-1}) at the level of peak heating (~5 km) at two different times for the 1-K WN3 thermal asymmetry simulations. (left) The fields at 0.5 h for (a) HIGRAD, (b) WRF, and (c) NUMA; (right) as in (left), but at 4 h.

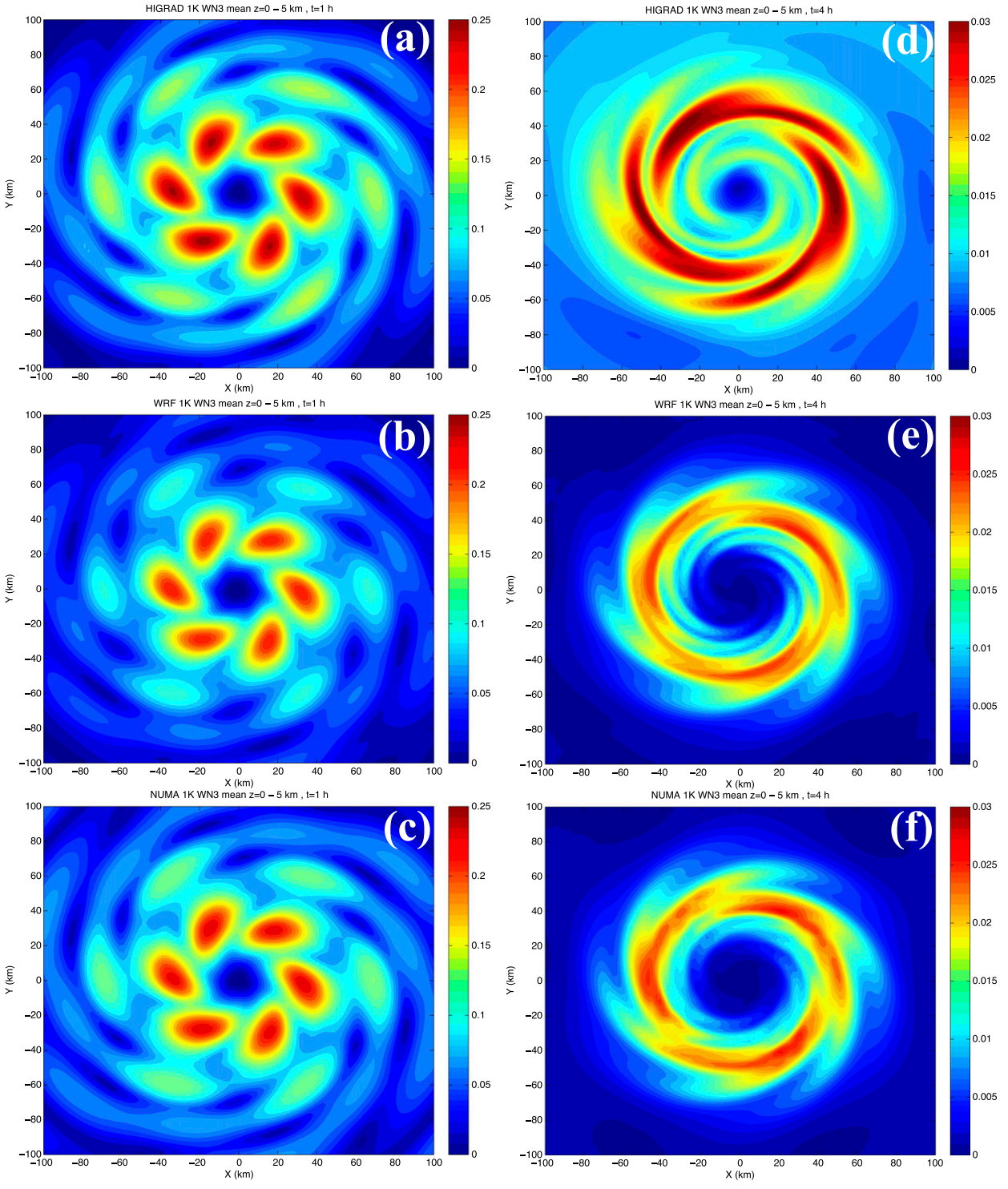

FIG. 4. Snapshots of perturbation horizontal wind speed ($m\,s^{-1}$) averaged between ~0- and 5-km heights at two different time periods for the 1-K WN3 thermal asymmetry simulations. (left) The fields at 1 h for (a) HIGRAD, (b) WRF, and (c) NUMA; (right) as in (left), but at 4 h.

the surrounding region. The structures and magnitudes from WRF and NUMA are similar to each other at this time. The results in Fig. 4 are consistent with the time series plots of maximum winds in Figs. 2c and 2d.

The absolute value of the impact ratio, |WN0/WN3|, for the 1-K anomaly in terms of maximum wind speed averaged over the last 2 h of the simulation (along with one standard deviation) is ~4 ± 0 for HIGRAD, ~20 ± 5 for WRF, and ~24 ± 13 for NUMA. The mean values are also listed in Table 2. This ratio was reported to be ~50 at 6 h in the work of NG03 in terms of maximum wind speed, with the 6-h WRF value equal to ~30 in this study. The differences between the NG03 WRF ratio and the one presented here are due to the slightly different initial vortex. The NG03 vortex had a broader tangential wind profile, which likely affected the axisymmetrization process to a small degree. The results of NG03 and further studies in NMS07 led the authors to conclude that asymmetric thermal forcing has a negligible effect on TC intensification. Note that NG03 and NMS07 typically found a weakening effect from asymmetric perturbations. However, they also found that changes to the vortex and the details of the heating distribution could result in intensification. The more robust result from these studies was the magnitude of the impact ratio.

The HIGRAD ratio is much smaller than that from either WRF or NUMA during the 4–6-h time period (see Table 2) for the 1-K perturbation, which is consistent with Fig. 2d. As shown above, the intensity response for the 1-K WN0 anomaly is essentially the same across the models, which means that differences in the asymmetric (1-K WN3) responses are the cause for the variability in the impact ratio.

Early in the course of this work, a large number of sensitivity tests were conducted to examine the cause of the differences between HIGRAD and WRF for the 1-K WN3 thermal anomaly. These tests included using different domains and resolutions (e.g., 1 km), changes to the boundary conditions and upper gravity wave absorber, using a dynamic initialization procedure, considering different wavenumber perturbations and locations, and varying the amount of explicit diffusion [see Guimond (2010) for details]. The very similar PV anomalies across models shown in Fig. 3 suggest that the disparities in vortex intensity described above are not due to differences in forcing of the vortex from eddy fluxes of PV or angular momentum; in fact, angular momentum budgets for the mean vortex intensity were computed (Guimond 2010), which showed this to be the case. Through these careful analyses, it became clear that we were dealing with a fundamental difference in the numerical algorithms that required additional analysis techniques and more model comparisons to understand the observed behavior.

b. *Larger-amplitude results*

Intensifying hurricanes often contain large pulses of latent heating associated with convective clouds in the eyewall region with rates of 200 K h^{-1} or more (Guimond et al. 2011). Observational studies have found that potential temperature perturbations in these clouds are ~5–10 K and persist for a finite amount of time (Houze et al. 2009). Here, we examine the impacts of larger-amplitude (10–50 K), impulsive perturbations keeping everything else the same as the small-amplitude experiment. Most of the amplitudes studied here represent a reasonable approximation to the study described above when considering the instantaneous nature of the perturbation. The largest amplitudes (e.g., 30–50 K) are examined to sample a broad range of model behavior.

Figure 5 shows the time series of perturbation maximum wind speed for a 20-K WN0 (Fig. 5a) and WN3 (Fig. 5c) perturbation along with the corresponding ratio plots comparing each model to WRF in Figs. 5b and 5d. The 20-K WN0 maximum wind speed plot (Fig. 5a) shows that all models produce a very similar axisymmetric response to the perturbation, consistent with the results from the 1-K WN0 case (Fig. 2a). The model wind speed ratios in Fig. 5b show values of ~1 throughout the simulation, with the exception of a brief spike in HIGRAD wind speeds at 1 h during the adjustment process. The response to the 20-K WN3 perturbation is very different. Both HIGRAD and NUMA (with either time integrator) show much larger responses to the asymmetric thermal than WRF at early times (<2 h) and at late times (~4–6 h), as illustrated in Figs. 5c and 5d. The HIGRAD and NUMA results are similar with the exception of some differences in the peaks and at late times (>5 h).

Figures 6a–d show the perturbation horizontal wind speed fields averaged over the ~0–5-km layer at 1 h into the 20-K WN3 simulations for HIGRAD, WRF, NUMA LF2, and NUMA ARK2B, respectively. The intense anomalies in the core are up to 2–3 m s^{-1} lower in WRF when compared to the other models, with HIGRAD and NUMA ARK2B producing the largest values. Outside of the core, three long tangential wavelength bands of elevated wind speed are evident, which are damped in WRF relative to the other models. Spectral kinetic energy budgets described later in the paper show this anomalous damping in WRF is largely due to differences in the flux of inertia–gravity wave energy. At 4 h into the simulations (Fig. 7), the wind speed fields have become much more axisymmetric, and WRF continues to show lower magnitudes compared to the other models. The HIGRAD

TABLE 2. Absolute value of the impact ratio, |WN0/WN3|, for impulsive thermal perturbations in each numerical model for various amplitudes. The ratio is listed as a 2-h average over the 4–6-h period rounded to the nearest whole number. This is reported in terms of either perturbation maximum wind speed or perturbation-integrated kinetic energy. The format is: wind ratio/kinetic energy ratio. The superscript letters indicate whether intensification (I) or weakening (W) was observed during this time period. The NUMA results use the LF2 time integrator, but similar results were obtained with the ARK2B scheme during this period.

Amplitude (K)	HIGRAD	WRF	NUMA
1	$4^{I}/7^{I}$	$20^{I}/1562^{I}$	$24^{I}/583^{I}$
10	$3^{I}/13^{I}$	$1596^{I}/40^{I}$	$17^{W}/36^{I}$
20	$5^{I}/13^{I}$	$36^{I}/39^{I}$	$9^{W}/16^{I}$
30	$28^{I}/13^{I}$	$63^{I}/24^{I}$	$13^{W}/25^{I}$
40	$3^{W}/217^{W}$	$13^{I}/495^{W}$	—
50	$3^{W}/10^{W}$	$3^{W}/6^{W}$	—

results (Fig. 7a) are a bit more similar to WRF (Fig. 7b) at this time, but both NUMA LF2 (Fig. 7c) and NUMA ARK2B (Fig. 7d) show significantly larger magnitudes in the core.

The absolute value of the impact ratio for the 20-K anomaly in terms of maximum wind speed averaged over the last 2 h of the simulation (along with one standard deviation) is $\sim 5 \pm 1$ for HIGRAD, $\sim 36 \pm 21$ for WRF, and $\sim 9 \pm 2$ for NUMA (see Table 2). It is clear from these results that WRF has a significantly reduced response to the WN3 thermal asymmetry, with HIGRAD and NUMA producing similar results. Table 2 also lists the impact ratio in terms of the perturbation integrated kinetic energy (IKE) per unit mass:

$$\mathrm{IKE} = 0.5 \iiint (u^2 + v^2)\, dx\, dy\, dz\,, \tag{11}$$

where the integral is evaluated across the full model domain in the horizontal and up to the gravity wave absorber in the vertical. For the 20-K anomaly, the impact ratio in terms of this intensity metric is $\sim 13 \pm 2$ for HIGRAD, $\sim 39 \pm 7$ for WRF, and $\sim 16 \pm 1$ for NUMA. The same core result is apparent, with the IKE metric as that described above for the maximum wind speeds indicating the robustness of the results.

Note that the 20-K WN3 anomaly resulted in intensification of the vortex in both HIGRAD and WRF in terms of either maximum wind speeds or IKE. The NUMA model produced weakening of the vortex for this anomaly in terms of maximum winds but did show intensification when reported in terms of IKE (see Table 2). The results for the 20-K anomaly were also examined using simulations at 400-m constant horizontal grid spacing in HIGRAD and WRF to compare to those obtained using 2-km spacing. The 400-m simulations produced a 10%–15% increase in IKE values in both HIGRAD and WRF such that the differences between the models were still apparent.

Other asymmetric thermal amplitudes were considered to sample a broad range of model behavior starting from 10 K and extending to 50 K with a 10-K increment. Note that NUMA results for the 40- and 50-K anomaly are not reported because instability developed in these cases as a result of the use of the free-slip setting at the surface coupled with the spatial discretization, which yields nearly inviscid conditions and large wind speeds.

Table 2 reports on a summary of these experiments through the impact ratio averaged over the last 2 h of the simulation in terms of either perturbation maximum winds speeds or perturbation IKE. The dominant sign of the asymmetric response is also listed. The axisymmetric perturbation response continued to show very similar results across the models for all thermal amplitudes, so the results in Table 2 really reflect the differences in the WN3 response. However, it is still useful to view the results in terms of the axisymmetric to asymmetric ratio. Note that sometimes very large impact ratios are found in each model, and this is due to a very small asymmetric response as the simulations attempt to reach a quasi-steady state. Table 3 shows only the asymmetric (WN3) results reported in terms of the perturbation IKE relative to WRF averaged over the entire 6-h simulations. This provides a concise summary of the overall vortex intensity and behavior of each model.

The bottom line message from Tables 2 and 3 is that WRF has a significantly muted response to the WN3 thermal perturbation expressed in terms of either intensity metric. The average impact ratio from WRF in the 1–40-K amplitude regime in terms of maximum wind speed is ~30–40 when ignoring the large value for the 10-K anomaly. HIGRAD produces the largest response to asymmetries with impact ratios averaging less than 10, with the most common value being 3. NUMA follows behind HIGRAD with average values of ~14–15. The WN3 response ratios in Table 3 show that both HIGRAD and NUMA are producing more kinetic energy than WRF between 1- and 20-K amplitudes, with HIGRAD again showing the largest values among models, extending up to the 40-K amplitude.

For WN3 thermal amplitudes between 1 and 30 K, both HIGRAD and WRF show intensification of the mean vortex in terms of either intensity metric, whereas NUMA shows some weakening effects for maximum wind speed but always intensification for IKE. For a WN3 thermal amplitude of 50 K, which is perhaps larger than what would occur in nature, the differences between HIGRAD and WRF are very small,

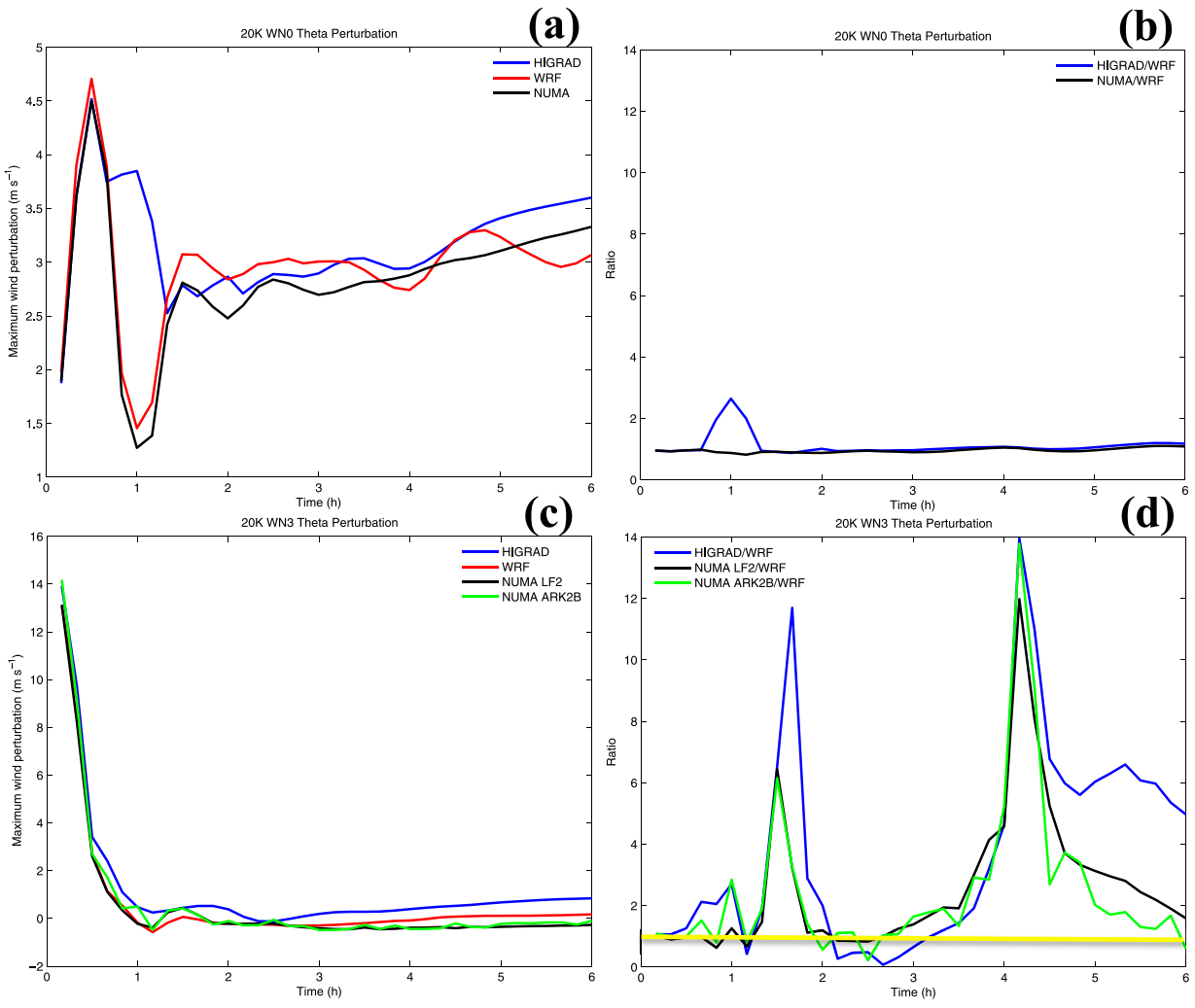

FIG. 5. Time series of (a),(c) maximum wind speed perturbation and (b),(d) maximum wind speed perturbation ratio relative to WRF for (top) the 20-K WN0 perturbation and (bottom) the 20-K WN3 perturbation. The results are reported at the lowest model level with a 10-min output interval. The yellow line in (d) helps to identify a ratio of one.

with both models showing an impact ratio of 3 and a weakening vortex.

Additional asymmetric wavenumber perturbations for the 10- and 20-K amplitudes, which are more realistic values, were tested using all three numerical models, and the results are listed in Table 4. The results from wavenumbers 4 and 5 are very consistent with those from wavenumber 3: WRF has the smallest impact for all asymmetries and amplitudes in this range, while HIGRAD produces the largest response, with NUMA following behind. In general, for the 10-K WN1 and WN2 asymmetries, the models produce more similar results, with the WN1 perturbation generating better agreement than WN2. When considering that the WN0 perturbation response was nearly the exact same across all models (see Figs. 2a,b, 5a,b), these results indicate that, as the scale of the thermal anomaly becomes larger, the models reach better agreement. Chagnon and Bannon (2001) showed using linear, analytical solutions that smaller-scale heating projects more strongly onto inertia–gravity wave energy, which suggests the importance of these waves and their numerical treatment for the problem studied here.

The overall impact of these results is that significant uncertainty exists in the numerical modeling of asymmetric TC intensification, at least for this idealized scenario. Both HIGRAD and NUMA indicate that asymmetric heating can have a substantial effect on the mean vortex intensification, whereas WRF shows a negligible effect, consistent with previous studies (e.g., NG03 and NMS07). An obvious question to ask from these results is: why is the vortex response to asymmetric

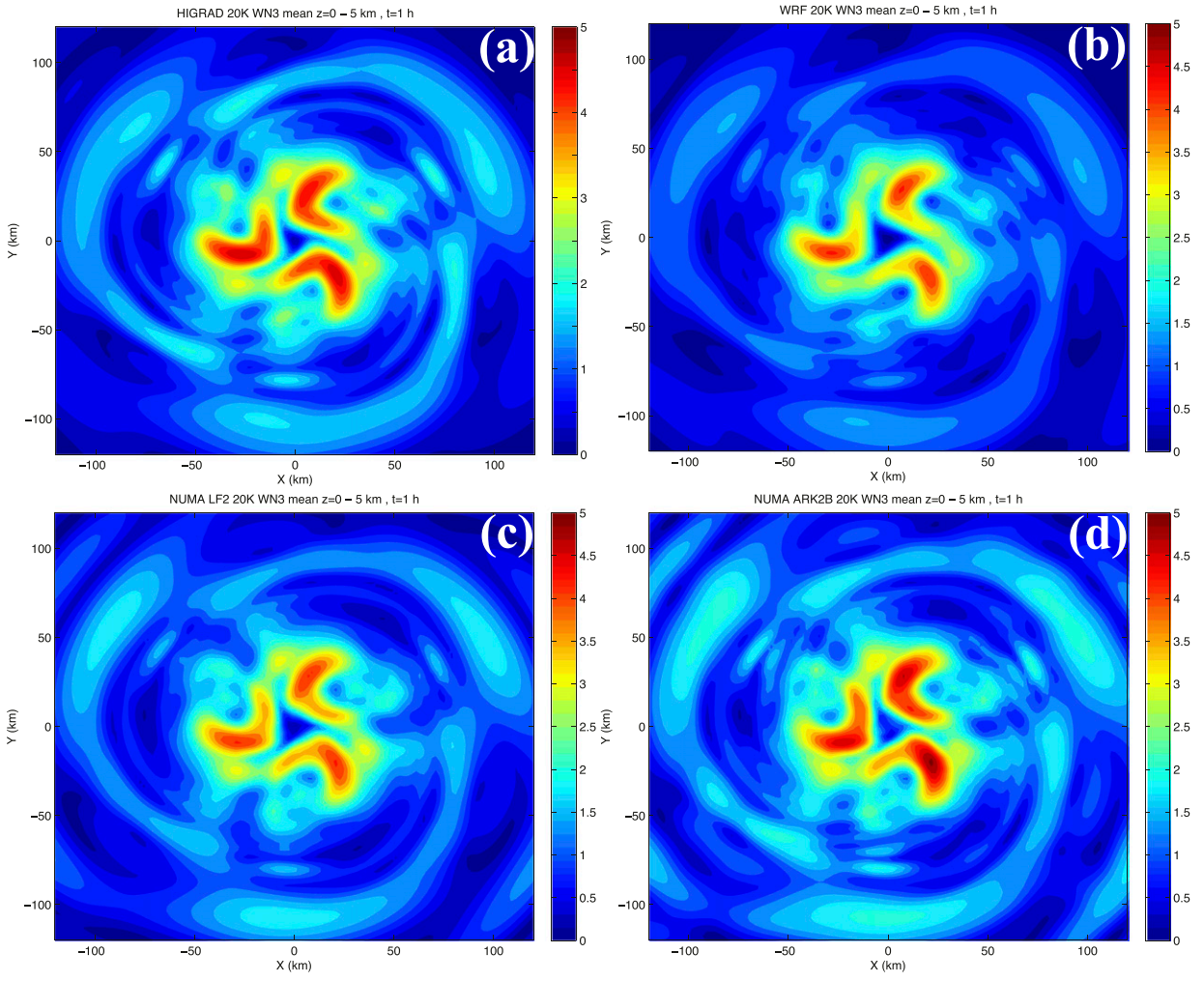

FIG. 6. Snapshots of perturbation horizontal wind speed (m s^{-1}) averaged between ~0- and 5- km heights at 1 h into the 20-K WN3 thermal asymmetry simulations for (a) HIGRAD, (b) WRF, (c) NUMA LF2, and (d) NUMA ARK2B.

thermal anomalies significantly muted in WRF, with some differences observed between HIGRAD and NUMA as well?

4. Spectral dynamics

To understand why HIGRAD and NUMA produce a stronger response to asymmetric thermal perturbations than WRF, the dynamics controlling the evolution of kinetic energy in spectral space is analyzed. Analyzing the spectral energetics of numerical models is a useful tool for understanding where energy resides and how it evolves in time across various length scales. Two WN3 perturbation amplitudes are studied: the 20-K anomaly, which produced significant differences between HIGRAD/NUMA and WRF, and the 50-K anomaly, which produced very similar results (see Table 2).

The discrete Fourier transform (DFT) of a variable Ψ in one spatial dimension x on a periodic domain with constant grid spacing can be written

$$\Psi(x_n) = \sum_{m=-Q}^{Q} F(k_m) e^{ik_m x_n} = F(0) + 2\left| \sum_{m=1}^{Q} F(k_m) e^{ik_m x_n} \right|, \tag{12}$$

where $x_n = L(n-1)/N$ is the physical position along the x dimension for index n over domain length L with N grid points, $k_m = 2\pi m/L$ is the wavenumber for index m, and Q represents the highest wavenumber index on the grid (length scale of twice the grid spacing). The complex Fourier coefficients are given by

$$F(k_m) = N^{-1} \sum_{n=1}^{N} \Psi(x_n) e^{-ik_m x_n}. \tag{13}$$

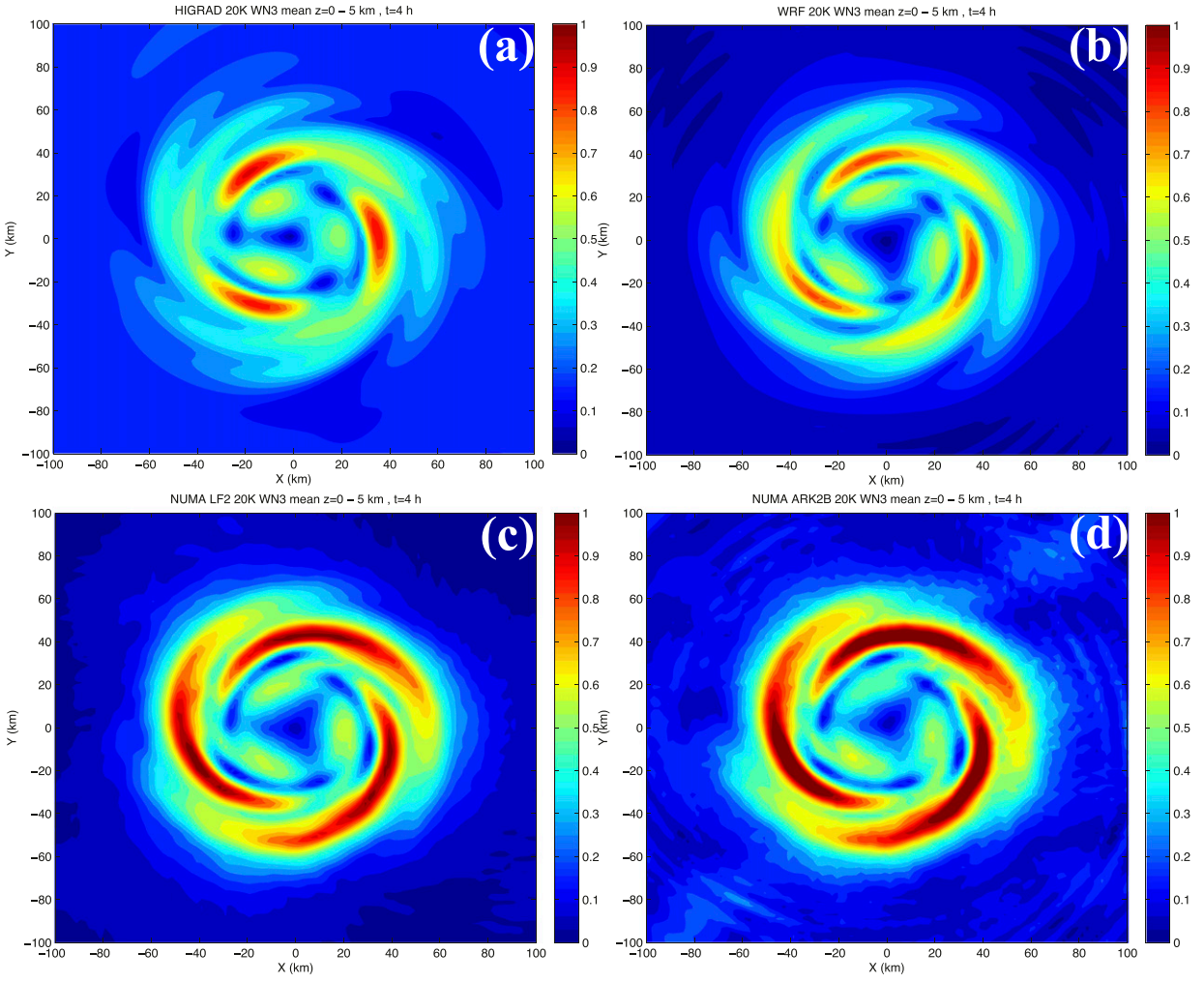

FIG. 7. As in Fig. 6, but at 4 h into the simulations.

In the calculation of the DFT, it is common practice to report on the positive wavenumbers only, which requires multiplying wavenumbers larger than 0 by a factor of 2 to account for the removal of the negative side of the spectrum. The DFT is computed for each horizontal velocity component along the x direction according to the equations above, and the kinetic energy spectrum per unit mass is calculated as follows:

$$E(k) = 0.5(\hat{u}^2 + \hat{v}^2), \tag{14}$$

where the hat over the velocity variables denotes the DFT field.

The kinetic energy spectrum computed along the x direction is averaged over the domain in the y direction

TABLE 3. Absolute value of the asymmetric (WN3) response ratio (relative to WRF), |Model/WRF|, in terms of perturbation-integrated kinetic energy [Eq. (11)] for impulsive thermal perturbations with various amplitudes in HIGRAD and NUMA. The ratio is listed as an average over the 6-h period along with one standard deviation.

Amplitude (K)	HIGRAD	NUMA LF2	NUMA ARK2B
1	103.0 ± 176.0	5.0 ± 9.0	6.0 ± 12.0
10	1.9 ± 1.1	1.2 ± 0.2	1.3 ± 0.5
20	2.3 ± 1.0	2.2 ± 0. 8	2.4 ± 0.8
30	1.6 ± 0.4	0.8 ± 0.3	0.9 ± 0.2
40	1.8 ± 2.1	—	—
50	1.2 ± 1.0	—	—

TABLE 4. As in Table 2, but replacing the denominator in the impact ratio with various asymmetric wavenumber perturbations.

Perturbation	HIGRAD	WRF	NUMA
10-K WN1	$1^{I}/7^{I}$	$2^{I}/21^{I}$	$3^{I}/16^{I}$
10-K WN2	$2^{I}/9^{I}$	$6^{I}/51^{I}$	$146^{I}/31^{I}$
10-K WN4	$3^{I}/9^{I}$	$29^{W}/377^{I}$	$15^{W}/34^{I}$
10-K WN5	$3^{I}/8^{I}$	$26^{W}/306^{I}$	$19^{W}/28^{I}$
20-K WN4	$4^{I}/10^{I}$	$341^{I}/37^{I}$	$13^{W}/15^{I}$
20-K WN5	$3^{I}/10^{I}$	$195^{I}/34^{I}$	$21^{W}/13^{I}$

and up to the start of the gravity wave damping layer in z for a specific time. This treatment is similar to other studies analyzing model spectra (e.g., Skamarock 2004). Note that spectra were also computed along the y direction and in both the x and y directions with two-dimensional DFTs, and similar results were obtained to those in x only.

Figure 8 shows the perturbation kinetic energy spectrum at four time intervals (0.5, 1, 3, and 6 h) for the 20-K WN3 simulations. At 0.5 h into the simulation (Fig. 8a), all models agree on the kinetic energy at scales greater than ~50 km, with some differences appearing below 50 km, such as the 20–50-km range (HIGRAD has the most energy), as well as near the tails of the spectrum (~10 km and below; NUMA has more energy). Note that the thermal anomaly initial condition has a scale of ~50 km. At 1 h into the simulation (Fig. 8b), some differences in the models are apparent at larger scales (up to 100 km), where NUMA has the most energy, and into the 20–50 km band, where HIGRAD continues to have the most energy. HIGRAD and WRF have a bit more damping in the $6\Delta x$–$7\Delta x$ region at 1 h and other times because of the sixth-order explicit filter in HIGRAD and the implicit filter in WRF. However, these scales have a minimal effect on the vortex scale intensity because energy is primarily transferred from the heating scale (~50 km) up to the larger vortex scales.

It is worthwhile to note that the 20-K anomaly fills out the mesoscale energy spectrum quicker and to a smaller scale than the 1-K anomaly (not shown), which is likely because of the excitation of nonlinearities for the 20-K anomaly case. The spectrum from the 20-K anomaly approaches the $k^{-5/3}$ theoretical slope at this time between roughly the 20- and 80-km wavelengths, whereas the 1-K anomaly resembled theory between ~50 and 80 km, albeit with a steeper slope. Note that the $k^{-5/3}$ theoretical slope of energy is more formally applicable to fully developed, three-dimensional, homogeneous turbulence (Kolmogorov 1941). While our simulations are idealized, the three-dimensional asymmetric heating perturbations generate three-dimensional motions with a variety of length scales, including inertia–gravity waves, which have been shown to energize the mesoscale kinetic energy spectrum (e.g., VanZandt 1982; Waite and Snyder 2009).

At 3 h (Fig. 8c), both HIGRAD and NUMA have more energy than WRF from ~50 km up to the largest scales of 800 km. This structure is also very similar at 6 h (Fig. 8d). The larger amount of kinetic energy at these scales in HIGRAD and NUMA is consistent with the larger intensity response reported in Table 2. At 3 and 6 h below the ~15–20 km wavelength, WRF and NUMA show more energy than HIGRAD, but this is not reflective of the vortex intensity. Scales below ~15 km are within the $6\Delta x$–$7\Delta x$ region and are more uncertain because of potential impacts from numerical noise. Note that the spectral slope of energy at 3 and 6 h shows similarities to theory in all models over a broad range of scales.

Figure 9 highlights the differences between models shown in Fig. 8 by plotting the ratio of spectral kinetic energy relative to that produced by WRF. Figure 9a shows that, at 0.5 h, HIGRAD produces a broad region of enhanced energy between ~15- and 50-km scales, with peak energy at a wavelength of ~15 km. This increase in energy moves upscale with time as the peak moves to a wavelength of ~25 km at 1 h and then spreads out to scales of ~50 km and larger at 3 and 6 h. The enhanced energy in HIGRAD amounts to approximately 2–3 times that from WRF, with the largest amount of energy occurring early in the simulation because of the nature of the impulsive initial condition.

The NUMA results with the LF2 time integrator are shown in Fig. 9b and are similar to those from HIGRAD. At 0.5 h, there is enhanced energy in NUMA at similar scales to HIGRAD, with peak values near 10-km wavelength. This enhanced energy moves upscale with time similar to what is observed with HIGRAD with peak energy 2–3 times that of WRF at scales greater than 50 km. The NUMA ARK2B results (Fig. 9c) show similar qualitative results to HIGRAD and NUMA LF2, but with much larger ratios (5–10 times those of WRF) at late times in the simulation (3–6 h). This indicates that part of the differences between the models is because of the level of numerical dissipation entering into the time integration scheme, since the ARK2B scheme is minimally dissipative.

For brevity, the perturbation spectral kinetic energy plots for the 50-K WN3 anomaly are not shown, which are mostly similar to the 20-K case. We note, however, that the 50-K anomaly produces a $k^{-5/3}$ energy slope quicker and fills out the spectrum to a smaller scale just as the 20-K anomaly did relative to the 1-K case. To highlight the differences between HIGRAD and WRF, we show the spectral kinetic energy ratio plots for the 50-K WN3 anomaly in Fig. 10. There is very little difference in kinetic energy at nearly all scales for the 50-K WN3 anomaly, with most ratios hovering around one in the first hour of the simulations. At 3 and 6 h, there are some small wavelength bands of increased energy in HIGRAD as well as some bands of decreased energy. Overall, the production of kinetic energy and vortex intensity (see Table 2) between HIGRAD and WRF is very similar.

The horizontal spectral kinetic energy tendency equation can be derived by differentiating Eq. (14) with respect to time and inserting the terms from the horizontal momentum equations (e.g., Koshyk and

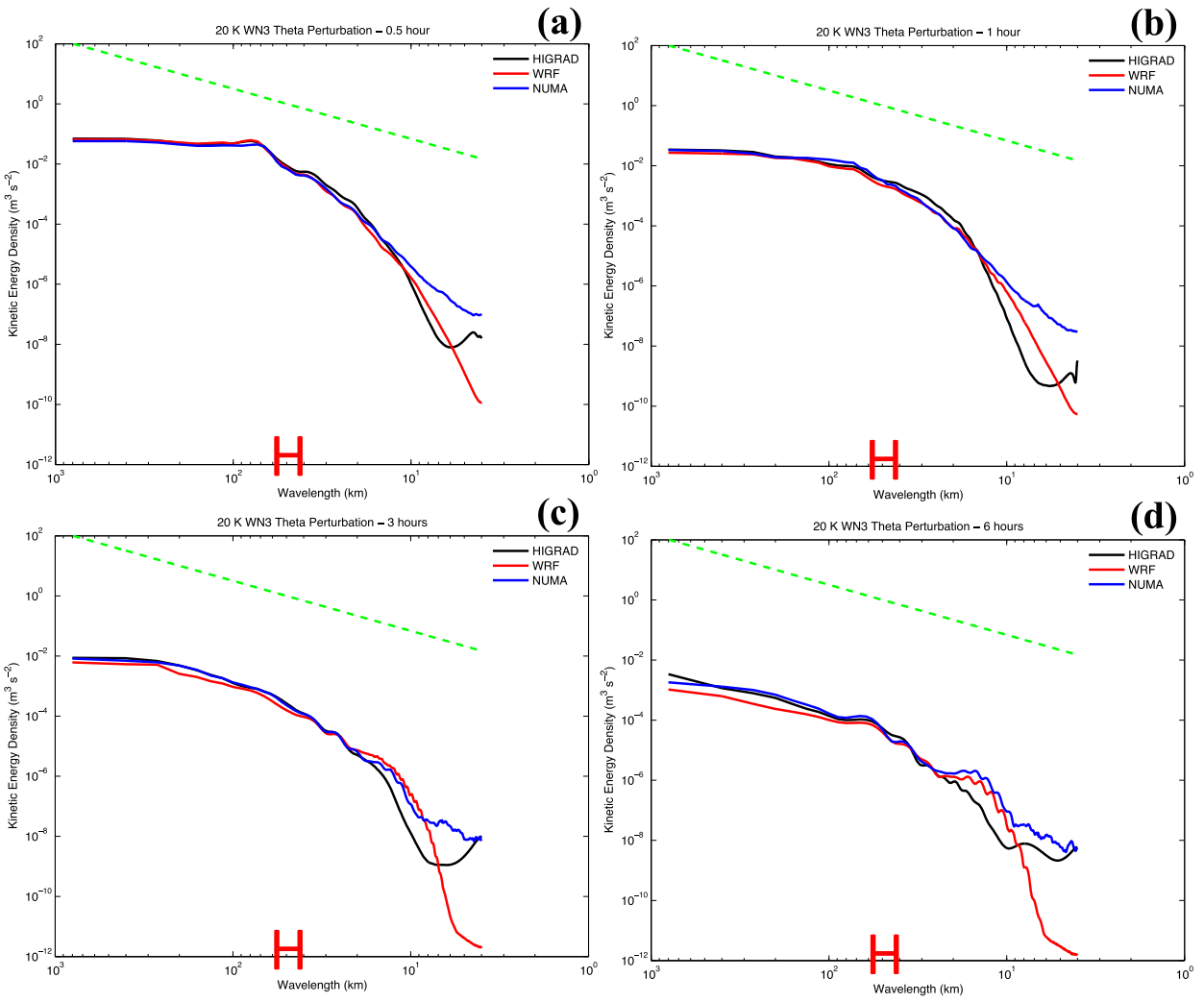

FIG. 8. Perturbation kinetic energy spectra for the 20-K WN3 theta perturbation in each model at (a) 0.5, (b) 1, (c) 3, and (d) 6 h. The green dashed line in each figure is the $k^{-5/3}$ mesoscale energy slope from turbulence theory. In this and subsequent figures, the red "H" highlights the approximate scale of the heating input.

Hamilton 2001; Waite and Snyder 2009). This procedure leads to the following equation:

$$\frac{\partial}{\partial t}E(k) = A(k) + P(k) + D(k), \tag{15}$$

where

$$A(k) = -\frac{1}{2}(\hat{\mathbf{v}}^* \cdot \widehat{\mathbf{ADV}} + \hat{\mathbf{v}} \cdot \widehat{\mathbf{ADV}}^*), \tag{16a}$$

$$P(k) = -\frac{1}{2}(\hat{\mathbf{v}}^* \cdot \widehat{\mathbf{PGF}} + \hat{\mathbf{v}} \cdot \widehat{\mathbf{PGF}}^*), \quad \text{and} \tag{16b}$$

$$D(k) = -\frac{1}{2}(\hat{\mathbf{v}}^* \cdot \widehat{\mathbf{DIFF}} + \hat{\mathbf{v}} \cdot \widehat{\mathbf{DIFF}}^*), \tag{16c}$$

The asterisks in Eqs. (16a)–(16c) represent complex conjugate terms and the boldface indicates horizontal vector quantities with $\mathbf{v}$ being the horizontal velocity vector. The total advection (**ADV**), pressure gradient force (**PGF**) and diffusion (**DIFF**) terms are labeled generically because in this paper they are replaced with the appropriate discretized terms inherent to each model (see Eqs. 1.1–1.2 for WRF, 2.1–2.2 for HIGRAD and 8.1–8.2 for NUMA). The momentum terms are output from each model and those terms coupled to either mass or density are decoupled to enable one-to-one comparisons across models. The pressure gradient force in the x direction, for example, is represented as $(1/\rho)(\partial p'/\partial x)$ in all models.

The first term on the right-hand side of Eq. (15) is the change in spectral kinetic energy due to the total (horizontal and vertical) transport across wavenumbers, which is a nonlinear contribution. The second term

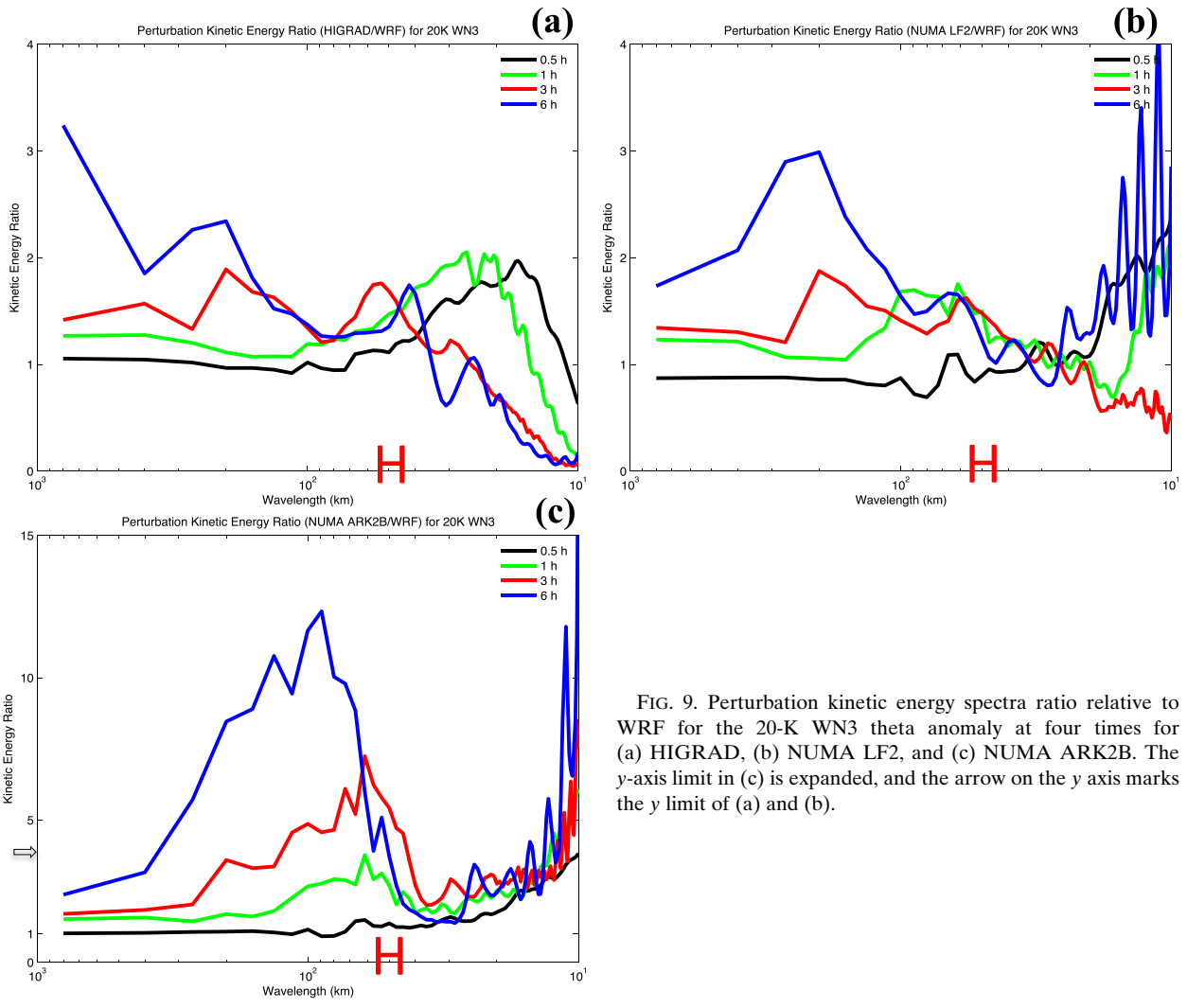

FIG. 9. Perturbation kinetic energy spectra ratio relative to WRF for the 20-K WN3 theta anomaly at four times for (a) HIGRAD, (b) NUMA LF2, and (c) NUMA ARK2B. The *y*-axis limit in (c) is expanded, and the arrow on the *y* axis marks the *y* limit of (a) and (b).

represents changes in energy due to horizontal pressure gradient force (hereinafter "pressure") effects, and the third term accounts for explicit subgrid-scale diffusion. The sum of these three terms describes the storage of kinetic energy in spectral space (left-hand-side term). Diffusion effects from the explicit sixth-order numerical filter in HIGRAD are omitted from this diagnostic analysis because they only affect the highest wavenumbers with minimal effects on the scales of interest (e.g., heating and vortex). In addition, contributions from the Coriolis force are very small and can be neglected.

Figure 11 shows the spectral kinetic energy budgets for the 20-K WN3 anomaly in each model averaged over the first 2 h of the simulation with a focus on scales of 30 km or more. The first 2 h is chosen as the averaging interval because most of the physics occurs in this period as a result of the nature of the impulsive initial condition. In HIGRAD (Fig. 11a), WRF (Fig. 11b), and NUMA LF2 (Fig. 11c), the storage term is positive at the heating input scale of ~50 km, extending down to 30 km and negative at all scales larger than 50 km. The NUMA ARK2B (Fig. 11d) simulation is also positive at 50 km, but there are significant regions of kinetic energy growth at larger scales (e.g., ~70–100 and ~150 km). Over the majority of the scales, WRF removes the most kinetic energy among the models with a large sink at 70-km wavelength. With the exception of the much smaller amplitudes, the structure of the storage term in WRF is similar to NUMA ARK2B. The HIGRAD and NUMA LF2 storage terms look very similar with some differences in amplitudes.

The majority of the changes in kinetic energy are controlled by the pressure term in each model, with WRF and NUMA ARK2B showing the largest contributions to the storage and HIGRAD and NUMA LF2

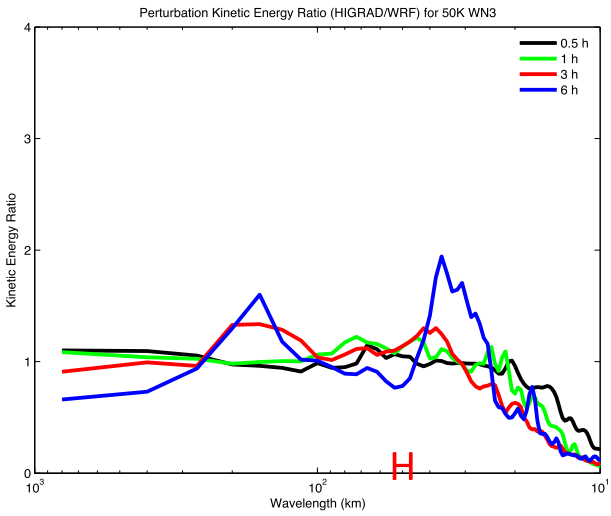

FIG. 10. Perturbation kinetic energy spectra ratio relative to WRF for the 50-K WN3 theta anomaly at four times for HIGRAD only.

the least. Note that the secondary increase in the storage and pressure term at ~100 km wavelength in all models (Fig. 11) is ultimately due to inertia–gravity wave activity and associated fluxes of energy during the adjustment process. More details on this process are discussed later in this section. An estimate of the deformation radius NH/I, where NH is the speed of an internal gravity wave (~60–100 m s^{-1}; Gill 1980) and I is the inertial frequency (10^{-3} s^{-1}), for this vortex adjustment problem is ~60–100 km. Considering the radial location of peak heating is at a radius of 40 km, the increase in the pressure/storage term around a wavelength of 100 km is generally consistent with a spreading and possible enhancement of kinetic energy controlled by the deformation radius.

The structure of the advective nonlinear terms in Fig. 11 is similar across all models. The horizontal and vertical fluxes have opposite signs over most wavelengths, but the horizontal component is larger and controls the sign of the total nonlinear flux of energy. From ~60- to 200-km wavelengths, the total nonlinear transfer of kinetic energy is negative, with positive values at larger scales. In the spectral domain, the advective nonlinearities only move energy across scales, which is approximately conservative (Koshyk and Hamilton 2001). This indicates that energy is being transferred from the scales of the heating up to the scales of the vortex, which is consistent with most models showing intensification of the vortex at later times (see Table 2). The total diffusion term, which is dominated by the vertical component, removes kinetic energy at all scales, with absolute values similar to the total nonlinear term.

After the first 2 h of the simulation, the changes in kinetic energy in all models become small and are controlled largely by vertical diffusion, with smaller impacts from the pressure and nonlinear terms (not shown). Subtle differences between these terms can lead to intensification versus weakening of the vortex at longer time periods (4–6 h), as illustrated in Table 2.

The spectral kinetic energy budget calculations indicate that HIGRAD and NUMA produce a stronger response to asymmetric thermal anomalies compared to WRF because the pressure term removes less energy in these models. In addition, in HIGRAD and NUMA LF2, the total advective nonlinearities (and diffusion) are able to play a larger role in the kinetic energy evolution compared to WRF and NUMA ARK2B because the pressure terms are not as dominant in these models. For example, HIGRAD (Fig. 11a) shows average (across wavelengths larger than the heating scale) differences between the storage and pressure terms of ~5–6 units, ~1–2 units for WRF (Fig. 11b), ~3–4 units for NUMA LF2 (Fig. 11c), and ~1 unit for NUMA ARK2B (Fig. 11d). The NUMA ARK2B simulation produces significantly more kinetic energy than WRF because the pressure term contributes to a positive increase or smaller decrease in energy.

An examination of nonlinear effects was tested by adding ±0.5 m s^{-1} random perturbations to the initial vortex wind fields in a ring centered on the radius of maximum winds. Simulations with the 20-K WN3 anomaly in HIGRAD and WRF (not shown) revealed an enhancement of the short-term (<2 h) intensity response in HIGRAD and essentially no change with WRF. The results of these tests are consistent with the discussion above in that WRF tends to damp out the effects of nonlinearities because of the anomalously large removal of kinetic energy from the pressure term. It is clear from this study, that the nonlinear transport of energy across wavenumbers can be an important effect leading to an enhancement of the impact of thermal asymmetries in hurricane intensification. Prior studies, such as NG03 and NMS07, only examined the linear and first-order, weakly nonlinear regimes and found asymmetries produced negligible effects.

Figure 12 shows the spectral kinetic energy budgets for the 50-K WN3 anomaly, comparing results between HIGRAD and WRF. The 50-K budget results show that the magnitudes and, to some extent, the structure of the pressure term is similar between HIGRAD (Fig. 12a) and WRF (Fig. 12b), which is in contrast to the 20-K results shown in Fig. 11. In addition, the storage of kinetic energy, which is also similar between models, is not completely dominated by the pressure term in

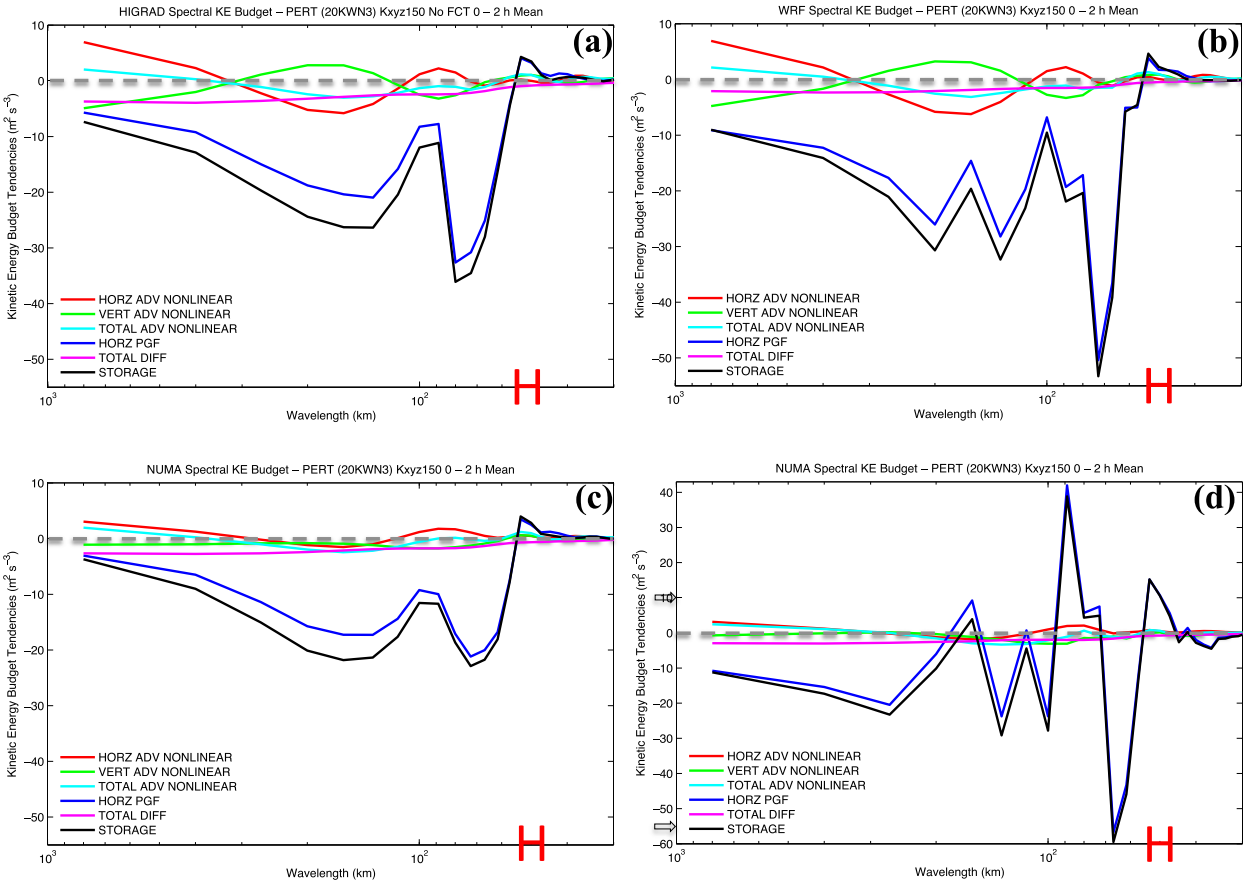

FIG. 11. Perturbation spectral kinetic energy budgets for the 20-K WN3 theta anomaly averaged over the first 2 h of the simulations for (a) HIGRAD, (b) WRF, (c) NUMA LF2, and (d) NUMA ARK2B. The *y*-axis limits in (d) are expanded, and the arrows on the *y* axis mark the limits in the other plots.

WRF (Fig. 12b), as it was for the 20-K anomaly (Fig. 11b). This allows the nonlinear transfer of kinetic energy to play more of a role in the kinetic energy evolution at various scales. In Fig. 12, both HIGRAD and WRF agree that the horizontal nonlinear transfer of energy is approximately upscale like that of the 20-K anomaly (Fig. 11), but the vertical component is negative at all scales and dominates the net transfer. This means that the 50-K WN3 thermal anomaly acts to remove energy from the vortex scales during the first 2 h of the simulations (largest changes in energy), which places the vortex on a significant weakening trend at longer time periods (see Table 2). The similarity of the spectral kinetic energy budgets between HIGRAD and WRF for the 50-K anomaly is consistent with the similar vortex impact ratios listed in Table 2.

Identification of the important pressure term helps us to understand the differences between the models, although additional insight into the physics of this ambiguous term would be more revealing. By applying the anelastic mass continuity equation (multiplied by pressure to enable flux form) and the hydrostatic equation to Eq. (16b), the pressure term can be rewritten as

$$\begin{aligned} P(k) &= -\frac{1}{2}(\hat{\mathbf{v}}^* \cdot \widehat{\mathbf{PGF}} + \hat{\mathbf{v}} \cdot \widehat{\mathbf{PGF}}^*) \\ &\cong -\frac{1}{2\overline{\rho}}\left[\frac{1}{\overline{\rho}}\frac{\partial}{\partial z}(\overline{\rho}\hat{w}^*\hat{p}) + g\hat{w}^*\hat{\rho} \right. \\ &\quad \left. + \frac{1}{\overline{\rho}}\frac{\partial}{\partial z}(\overline{\rho}\hat{w}\hat{p}^*) + g\hat{w}\hat{\rho}^*\right], \end{aligned} \tag{17}$$

where the bar over density represents the hydrostatically balanced reference state, which is a function of height only. The derivation of Eq. (17) and the discussion of the terms below are similar to those of Koshyk and Hamilton (2001) and Waite and Snyder (2009), although these studies used the Boussinesq approximation instead of the anelastic used here. The first term on the right-hand side is the vertical divergence of the vertical pressure flux, which is related to the flux of inertia–gravity wave energy. The second term represents the conversion

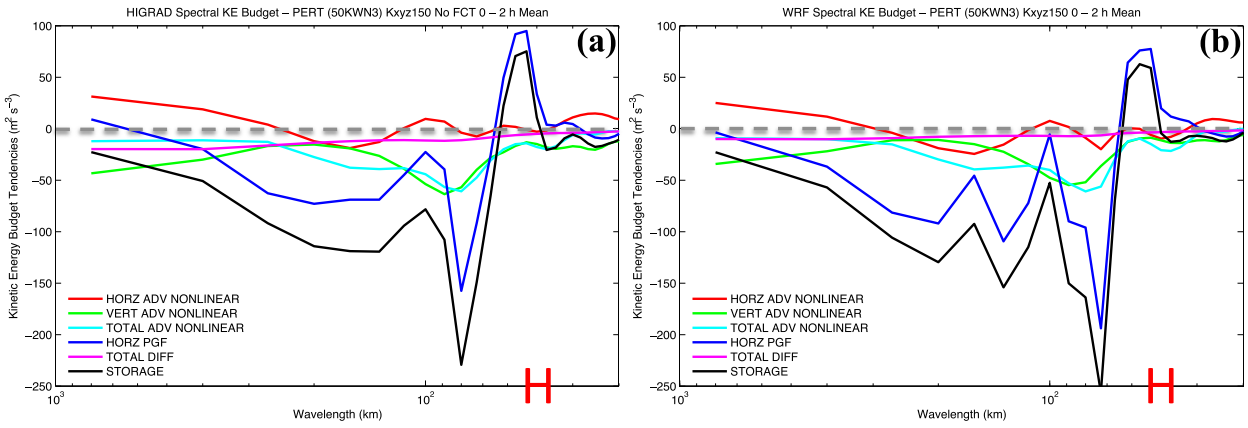

FIG. 12. As in Fig. 10, but for the 50-K WN3 anomaly for (a) HIGRAD and (b) WRF.

from potential to kinetic energy associated with the introduction of the thermal perturbation and will be referred to as the buoyancy flux. The third and fourth terms are the complex conjugate expressions for the first and second terms, respectively.

Figure 13 shows the results of the pressure term decomposition for the 20-K WN3 thermal anomaly in each model averaged over the first 2 h of the simulations. Note that the reconstructed pressure terms from each model in Fig. 13 are approximations (e.g., hydrostatic) to the actual terms shown in Fig. 11, and some relatively minor differences are found. For example, the actual pressure term is a bit larger (more negative) for WRF in Fig. 11b than the reconstructed term in Fig. 13b, and the NUMA ARK2B results show some differences as well. Generally, however, the pressure decompositions are reliable for understanding the model energetics.

In each model, both the vertical pressure flux divergence and the buoyancy flux have similar contributions to the pressure term, but with opposite signs. The largely positive contribution from the vertical pressure flux divergence term indicates that kinetic energy is being supplied at most scales by the convergence of inertia–gravity wave energy fluxes. The buoyancy flux is always negative and slightly larger than the inertia–gravity wave contribution, which determines the sign of the pressure term, except in the case of NUMA ARK2B (Fig. 13d). A negative buoyancy flux is consistent with the conversion of kinetic energy to potential energy through adiabatic vertical motions in the dry simulations.

The buoyancy flux terms in HIGRAD (Fig. 13a), WRF (Fig. 13b), and NUMA LF2 (Fig. 13c) are mostly similar to each other, whereas the vertical pressure flux divergence shows larger differences between these models. In WRF, the vertical pressure flux divergence term has significant negative values just upscale from the heating input, which contributes to the large removal of kinetic energy observed at these scales in the actual pressure term (Fig. 11b). The NUMA ARK2B results in Fig. 13d have larger magnitudes and, to some extent, different structure than the other models, which is because of the use of the minimally dissipative ARK2B time integration scheme and its effects on the energetics of inertia–gravity waves. The introduction of ''noise'' from the reflection of gravity waves at the model top, for instance, is more possible using this time integrator.

Overall, the results of the pressure term decomposition indicate that, from a physical perspective, the differences in kinetic energy and ultimately the vortex response to asymmetric thermal perturbations across the models are mostly due to inertia–gravity waves and their fluxes of energy. These waves and the pressure terms in the governing equations that produce them are handled mostly implicitly in the numerical solutions of each model. The differences in kinetic energy between NUMA LF2 and ARK2B indicate that diffusion in the time integrator for the implicit modes likely plays an important role in these results. The use of the C grid in WRF is also a potential culprit for the anomalous dissipation, and the interaction of spatial and temporal discretization errors for this problem may be important, which requires further study.

5. Summary, conclusions, and implications

In this paper, the fundamental dynamics of TC intensification was analyzed by considering axisymmetric and asymmetric impulsive thermal perturbations to balanced, TC-like vortices using the dynamic cores of three different numerical models. Previous studies of this problem by NG03 used the community nonlinear atmospheric WRF Model to validate predictions made by a linear model. The NG03 results showed that small-amplitude

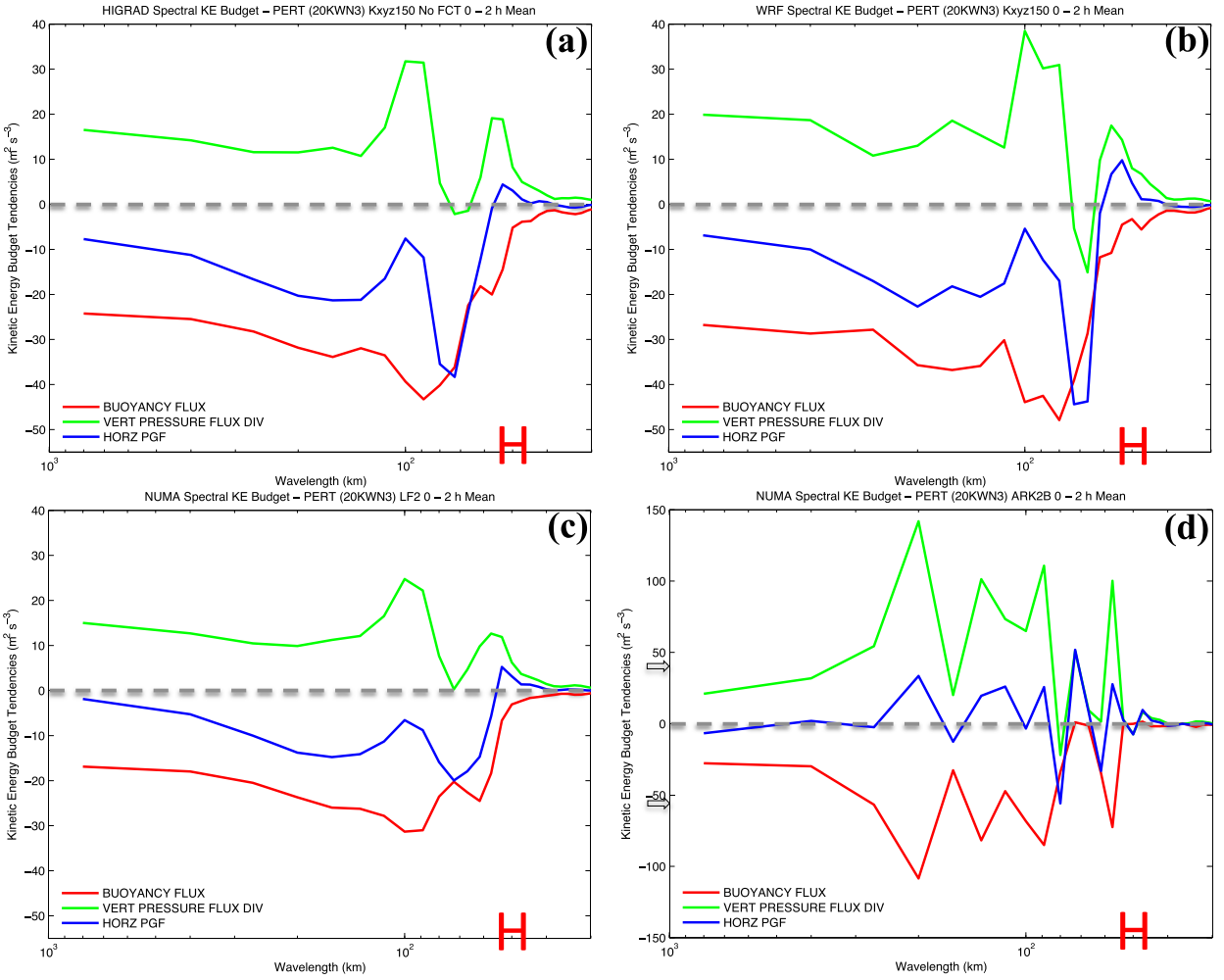

FIG. 13. Decomposition of the pressure term contribution to the spectral kinetic energy budget for the 20-K WN3 thermal averaged over the first 2 h of the simulations. Results are shown for (a) HIGRAD, (b) WRF, (c) NUMA LF2, and (d) NUMA ARK2B. The dashed gray line in each panel highlights the zero tendency line. The *y*-axis limits in (d) are expanded, and arrows placed on the *y* axis mark the limits in the other plots.

(1 K) purely asymmetric thermal anomalies have a negligible and most often negative effect on the vortex intensification. These results were analyzed further with time evolving heating in a linear model by NMS07, which showed consistent effects with those of NG03.

In the current study, asymmetric thermal perturbations are also shown to have a negligible effect on intensification using WRF, but the majority of results from two other nonlinear numerical models (HIGRAD and NUMA) show significant differences with asymmetries producing substantial effects. For asymmetric (wavenumbers 3–5) perturbation amplitudes between 1 and 40 K, the ratio of axisymmetric to asymmetric effects, reported in terms of perturbation maximum wind speeds, was most often ~30–40 in WRF, ~14–15 in NUMA, and ~3–5 in HIGRAD. Similar differences were also found in terms of domain-integrated kinetic energy. Axisymmetric perturbations produced very similar results across all models, and there were indications that the model differences increased as the scale of the perturbation decreased. While axisymmetric thermal forcing will always produce a larger intensity response because of the larger net energy input, the results presented here indicate that asymmetric heating can produce important effects. For asymmetric amplitudes of 30 K and below, the signs of these effects are most often consistent across models, with the results showing intensification of the mean vortex. However, some weakening effects were also observed.

The spectral kinetic energy characteristics of the vortex response to asymmetric thermal perturbations were analyzed to understand the nature of the differences between the models. This analysis showed that HIGRAD and NUMA produced considerably more

kinetic energy than WRF for the 20-K WN3 anomaly, with the increased energy originating around the scales of the heating and propagating up to the vortex scale with time because of nonlinear effects. Spectral kinetic energy budgets revealed that much of this anomalous damping in WRF is due to the increased removal of kinetic energy from the divergence of the vertical pressure flux, which is related to the flux of inertia–gravity wave energy. For very large thermal amplitudes (50-K WN3), the anomalous removal of kinetic energy is much smaller, resulting in good agreement between the models.

The idealized nature of the problem studied (e.g., dry, no boundary layer, and constant eddy viscosities), coupled with the use of the exact same initial and boundary conditions and similar governing equations isolates the model differences to the numerical scheme. This means that, for asymmetric impulsive thermal anomalies, the WRF Model has significantly more numerical dissipation than HIGRAD and NUMA. The results from the spectral kinetic energy budget analysis and the observation that axisymmetric thermal perturbations produced very similar results across models indicates that the numerical treatment of small-scale processes that project strongly onto inertia–gravity wave energy are responsible for these differences.

We hypothesize that the use of the C grid in WRF, which adds spatial diffusion, coupled with potential diffusion entering into the time integration scheme for the fast modes (horizontally explicit and vertically implicit) are possible culprits for this anomalous diffusion. The sensitivity of the spectral kinetic energy results to diffusion in the time integrator was tested with NUMA, which showed significant differences in the amount of energy and role of the pressure terms.

We emphasize that, because no analytical solution exists for this problem, we do not know which model solution is correct in the absolute sense. An attempt was made to address the convergence of the codes by performing simulations at horizontal grid spacing of 400 m (a factor-of-5 increase in resolution), but the same core result was found. Further grid refinements may be necessary, but they are unable to be addressed here.

The implications of this research are the following. There is clearly sensitivity to the chosen numerical scheme for the asymmetric thermal perturbations, which casts considerable doubt on the role of asymmetric dynamics in TC intensification. For similar idealized simulations described here, users of the WRF Model are likely to see a significantly muted intensity response to asymmetric heating in the core of a hurricane. Other models with similar numerical schemes to HIGRAD and NUMA will likely see a more energetic, enhanced response from asymmetric perturbations. While much of the response to asymmetric perturbations caused intensification of the vortex in this study, significant weakening was sometimes found as well. Currently, we are examining how far the results presented in this study extend when considering a more realistic regime characterized by observationally based heating, the addition of moisture, and turbulence-resolving resolution.

Acknowledgments. The first author would like to thank the Institute of Geophysics, Planetary Physics, and Signatures (IGPPS) at Los Alamos National Laboratory for supporting this work. The first author thanks Dr. David Nolan for many useful comments on the work and for providing his initial conditions. The first author also thanks Dr. Michael Waite for discussions on the spectral dynamics portion of the study. We thank Dr. Michal Kopera for assistance with NUMA parallel I/O. Input from Dr. Paul Reasor on early versions of this work was valuable. In addition, we thank Dr. George Bryan, Dr. Bill Skamarock, and Dr. Mike Montgomery for their comments. The contribution of SM and FXG was supported by the Office of Naval Research through program element PE-0602435. Finally, we thank three anonymous reviewers for their constructive criticism, which helped improve the conclusions and clarity of the paper.

REFERENCES

Chagnon, J. M., and P. R. Bannon, 2001: Hydrostatic and geostrophic adjustment in a compressible atmosphere: Initial response and final equilibrium to an instantaneous localized heating. *J. Atmos. Sci.*, **58**, 3776–3792, doi:10.1175/1520-0469(2001)058<3776:HAGAIA>2.0.CO;2.

Eliassen, A., 1951: Slow thermally or frictionally controlled meridional circulation in a circular vortex. *Astrophys. Norv.*, **5**, 19–60.

Emanuel, K. A., 1986: An air–sea interaction theory for tropical cyclones. Part I: Steady-state maintenance. *J. Atmos. Sci.*, **43**, 2044–2061, doi:10.1175/1520-0469(1986)043<0585:AASITF>2.0.CO;2.

Farrell, B. F., 1982: The initial growth of disturbances in a baroclinic flow. *J. Atmos. Sci.*, **39**, 1663–1686, doi:10.1175/1520-0469(1982)039<1663:TIGODI>2.0.CO;2.

Gill, A. E., 1980: Some simple solutions for heat-induced tropical circulation. *Quart. J. Roy. Meteor. Soc.*, **106**, 447–462, doi:10.1002/qj.49710644905.

Giraldo, F. X., and M. Restelli, 2008: A study of spectral element and discontinuous Galerkin methods for the Navier–Stokes equations in nonhydrostatic mesoscale atmospheric modeling: Equation sets and test cases. *J. Comput. Phys.*, **227**, 3849–3877, doi:10.1016/j.jcp.2007.12.009.

——, J. F. Kelly, and E. M. Constantinescu, 2013: Implicit–explicit formulations of a three-dimensional Nonhydrostatic Unified Model of the Atmosphere (NUMA). *SIAM J. Sci. Comput.*, **35**, 1162–1194, doi:10.1137/120876034.

Guimond, S. R., 2010: Tropical cyclone inner-core dynamics: A latent heat retrieval and its effects on intensity and structure change; and the impacts of effective diffusion on the ax-

isymmetrization process. Ph. D. dissertation, Dept. of Earth, Ocean and Atmospheric Science, Florida State University, 132 pp. [Available online at http://diginole.lib.fsu.edu/etd/3920.]

——, M. A. Bourassa, and P. D. Reasor, 2011: A latent heat retrieval and its effects on the intensity and structure change of Hurricane Guillermo (1997). Part I: The algorithm and observations. *J. Atmos. Sci.*, **68**, 1549–1567, doi:10.1175/2011JAS3700.1.

Houze, R. A., Jr., W.-C. Lee, and M. M. Bell, 2009: Convective contribution to the genesis of Hurricane Ophelia (2005). *Mon. Wea. Rev.*, **137**, 2778–2800, doi:10.1175/2009MWR2727.1.

Jordan, C. L., 1958: Mean soundings for the West Indies area. *J. Meteor.*, **15**, 91–97, doi:10.1175/1520-0469(1958)015<0091:MSFTWI>2.0.CO;2.

Kelly, J. F., and F. X. Giraldo, 2012: Continuous and discontinuous Galerkin methods for a scalable three-dimensional nonhydrostatic atmospheric model: Limited-area mode. *J. Comput. Phys.*, **231**, 7988–8008, doi:10.1016/j.jcp.2012.04.042.

Klemp, J. B., and R. Wilhelmson, 1978: The simulation of three-dimensional convective storm dynamics. *J. Atmos. Sci.*, **35**, 1070–1096, doi:10.1175/1520-0469(1978)035<1070:TSOTDC>2.0.CO;2.

Knievel, J. C., G. H. Bryan, and J. P. Hacker, 2007: Explicit numerical diffusion in the WRF Model. *Mon. Wea. Rev.*, **135**, 3808–3824, doi:10.1175/2007MWR2100.1.

Kolmogorov, A. N., 1941: The local structure of turbulence in incompressible viscous fluid for very large Reynolds number. *Dokl. Akad. Nauk SSSR*, **30**, 301–305.

Koshyk, J. N., and K. Hamilton, 2001: The horizontal kinetic energy spectrum and spectral budget simulated by a high-resolution troposphere–stratosphere–mesosphere GCM. *J. Atmos. Sci.*, **58**, 329–348, doi:10.1175/1520-0469(2001)058<0329:THKESA>2.0.CO;2.

Laprise, R., 1992: The Euler equations of motion with hydrostatic pressure as an independent variable. *Mon. Wea. Rev.*, **120**, 197–207, doi:10.1175/1520-0493(1992)120<0197:TEEOMW>2.0.CO;2.

Leonard, B., and J. Drummond, 1995: Why you should not use "hybrid", "power-law" or related exponential schemes for convective modeling—There are much better alternatives. *Int. J. Numer. Methods Fluids*, **20**, 421–442, doi:10.1002/fld.1650200602.

Melander, M. V., J. C. McWilliams, and N. J. Zabusky, 1987: Axisymmetrization and vorticity-gradient intensification of an isolated two-dimensional vortex through filamentation. *J. Fluid Mech.*, **178**, 137–159, doi:10.1017/S0022112087001150.

Montgomery, M. T., and R. J. Kallenbach, 1997: A theory for vortex Rossby waves and its application to spiral bands and intensity changes in hurricanes. *Quart. J. Roy. Meteor. Soc.*, **123**, 435–465, doi:10.1002/qj.49712353810.

——, and J. Enagonio, 1998: Tropical cyclogenesis via convectively forced vortex Rossby waves in a three-dimensional quasi-geostrophic model. *J. Atmos. Sci.*, **55**, 3176–3207, doi:10.1175/1520-0469(1998)055<3176:TCVCFV>2.0.CO;2.

——, M. E. Nicholls, T. A. Cram, and A. Saunders, 2006: A vortical hot tower route to tropical cyclogenesis. *J. Atmos. Sci.*, **63**, 355–386, doi:10.1175/JAS3604.1.

Nolan, D. S., 2011: Evaluating environmental favorableness for tropical cyclone development with the method of point-downscaling. *J. Adv. Model. Earth Syst.*, **3**, 1–28, doi:10.1029/2011MS000063.

——, and B. F. Farrell, 1999: The intensification of two-dimensional swirling flows by stochastic asymmetric forcing. *J. Atmos. Sci.*, **56**, 3937–3962, doi:10.1175/1520-0469(1999)056<3937:TIOTDS>2.0.CO;2.

——, and M. T. Montgomery, 2002: Nonhydrostatic, three-dimensional perturbations to balanced, hurricane-like vortices. Part I: Linearized formulation, stability, and evolution. *J. Atmos. Sci.*, **59**, 2989–3020, doi:10.1175/1520-0469(2002)059<2989:NTDPTB>2.0.CO;2.

——, and L. D. Grasso, 2003: Three-dimensional, nonhydrostatic perturbations to balanced, hurricane-like vortices. Part II: Symmetric response and nonlinear simulations. *J. Atmos. Sci.*, **60**, 2717–2745, doi:10.1175/1520-0469(2003)060<2717:NTPTBH>2.0.CO;2.

——, Y. Moon, and D. P. Stern, 2007: Tropical cyclone intensification from asymmetric convection: Energetics and efficiency. *J. Atmos. Sci.*, **64**, 3377–3405, doi:10.1175/JAS3988.1.

Persing, J., M. T. Montgomery, J. C. McWilliams, and R. K. Smith, 2013: Asymmetric and axisymmetric dynamics of tropical cyclones. *Atmos. Chem. Phys.*, **13**, 12 299–12 341, doi:10.5194/acp-13-12299-2013.

Reasor, P. D., M. T. Montgomery, F. D. Marks Jr., and J. F. Gamache, 2000: Low- wavenumber structure and evolution of the hurricane inner core observed by airborne dual-Doppler radar. *Mon. Wea. Rev.*, **128**, 1653–1680, doi:10.1175/1520-0493(2000)128<1653:LWSAEO>2.0.CO;2.

Reisner, J. M., V. A. Mousseau, A. A. Wyszogrodzki, and D. A. Knoll, 2005: An implicitly balanced hurricane model with physics-based preconditioning. *Mon. Wea. Rev.*, **133**, 1003–1022, doi:10.1175/MWR2901.1.

Rotunno, R., and K. A. Emanuel, 1987: An air–sea interaction theory for tropical cyclones. Part II: Evolutionary study using a nonhydrostatic axisymmetric numerical model. *J. Atmos. Sci.*, **44**, 542–561, doi:10.1175/1520-0469(1987)044<0542:AAITFT>2.0.CO;2.

Schubert, W. H., M. T. Montgomery, R. K. Taft, T. A. Guinn, S. R. Fulton, J. P. Kossin, and J. P. Edwards, 1999: Polygonal eyewalls, asymmetric eye contraction, and potential vorticity mixing in hurricanes. *J. Atmos. Sci.*, **56**, 1197–1223, doi:10.1175/1520-0469(1999)056<1197:PEAECA>2.0.CO;2.

Shapiro, L. J., and H. E. Willoughby, 1982: The response of balanced hurricanes to local sources of heat and momentum. *J. Atmos. Sci.*, **39**, 378–394, doi:10.1175/1520-0469(1982)039<0378:TROBHT>2.0.CO;2.

Skamarock, W. C., 2004: Evaluating mesoscale NWP models using kinetic energy spectra. *Mon. Wea. Rev.*, **132**, 3019–3032, doi:10.1175/MWR2830.1.

——, and J. B. Klemp, 2008: A time-split nonhydrostatic atmospheric model for weather research and forecasting applications. *J. Comput. Phys.*, **227**, 3465–3485, doi:10.1016/j.jcp.2007.01.037.

——, and Coauthors, 2008: A description of the Advanced Research WRF version 3. NCAR Tech. Note NCAR/TN-475+STR, 113 pp., doi:10.5065/D68S4MVH.

Smith, G. B., and M. T. Montgomery, 1995: Vortex axisymmetrization: Dependence of azimuthal wave-number or asymmetric radial structure changes. *Quart. J. Roy. Meteor. Soc.*, **121**, 1615–1650, doi:10.1002/qj.49712152707.

VanZandt, T. E., 1982: A universal spectrum of buoyancy waves in the atmosphere. *Geophys. Res. Lett.*, **9**, 575–578, doi:10.1029/GL009i005p00575.

Waite, M. L., and C. Snyder, 2009: The mesoscale kinetic energy spectrum of a baroclinic life cycle. *J. Atmos. Sci.*, **66**, 883–901, doi:10.1175/2008JAS2829.1.

Wicker, L., and W. Skamarock, 2002: Time-splitting methods for elastic models using forward time schemes. *Mon. Wea. Rev.*, **130**, 2088–2097, doi:10.1175/1520-0493(2002)130<2088:TSMFEM>2.0.CO;2.

Xue, M., 2000: High-order monotonic numerical diffusion and smoothing. *Mon. Wea. Rev.*, **128**, 2853–2864, doi:10.1175/1520-0493(2000)128<2853:HOMNDA>2.0.CO;2.

Yang, B., Y. Wang, and B. Wang, 2007: The effect of internally generated inner-core asymmetries on tropical cyclone potential intensity. *J. Atmos. Sci.*, **64**, 1165–1188, doi:10.1175/JAS3971.1.